# Metal remobilization and ore-fluid perturbation during episodic replacement of auriferous pyrite from an epizonal orogenic gold deposit

Ya-Fei Wu [a,b], Katy Evans [b], Jian-Wei Li [a,*], Denis Fougerouse [b], Ross R. Large [c], Paul Guagliardo [d]

[a] *State Key Laboratory of Geological Processes and Mineral Resources and School of Earth Resources, China University of Geosciences, Wuhan, Hubei Province 430074, China*

[b] *School of Earth and Planetary Sciences, The Institute for Geoscience Research (TIGeR), Curtin University, GPO Box U1987, Perth, WA 6845, Australia*

[c] *ARC Centre of Excellence in Ore Deposits (CODES), School of Physical Sciences, University of Tasmania, Private Bag 79, Hobart, Tasmania 7001, Australia*

[d] *Centre for Microscopy, Characterisation and Analysis, The University of Western Australia, 35 Stirling Highway, Crawley, WA 6009, Australia*

[*] Corresponding author:

Tel.: +86 27 67883653; Fax: +86 27 67885096

E-mail address: jwli@cug.edu.cn

## Abstract

Mineral-scale episodic replacement of auriferous pyrite by texturally-complex pyrite, marcasite and minor arsenopyrite occurred in breccia ores from the Daqiao epizonal orogenic gold deposit, West Qinling Orogen, China. This study uses a novel combination of laser ablation-inductively coupled plasma-mass spectrometry (LA-ICP-MS), Nanoscale secondary ion mass spectrometry (NanoSIMS), and secondary ion mass spectrometry (SIMS) to investigate the remobilization and re-concentration of gold and other trace elements during this complex replacement process and the probable mechanism. Several lines of evidence including some degree of preservation of external morphology, sharp contacts and compositional differences between the parent pyrite and product pyrite and marcasite, and reaction-induced porosity suggest that the replacement of parent pyrite proceeds via a two-step replacement via a dissolution and reprecipitation mechanism, plus an additional marcasite overgrowth. During the replacement of euhedral pyrite, depletion of gold and other trace elements (Te, Se, Zn, Co, Tl, Ni, W, and As) in porous product pyrite relative to its precursor indicate exsolution and remobilization of these metals from crystal lattice of the original pyrite. In the subsequent replacement of porous pyrite by two types of marcasite and minor arsenopyrite, euhedral product marcasite contains low contents of trace elements, possibly due to high metal solubility in the acidic fluids favorable for marcasite precipitation. The complex-zoned marcasite significantly enriched in gold and other metals relative to porous pyrite (W, Tl, As, Sb, Ag, Se, and Zn) is thought to have formed via precipitation triggered by further oxidation and/or

immediate reduction in threshold supersaturation. Dissolution of the impurity-rich pyrite and precipitation of new pyrite and marcasite generations could have occurred at low pH plus high concentrations of dissolved $Fe^{2+}$ condition caused by partial oxidation of aqueous $H_2S$ and/or $S^{2-}$ in ore fluids. The fluid oxidation is evidenced by a general decreasing trend of $\delta^{34}S$ values from the parent euhedral pyrite, to product porous pyrite, euhedral marcasite, and complex-zoned marcasite. The isotopic results are consistent with ore fluid oxidation controlled by pressure fluctuations during multistage hydraulic fracturing in a fault-valve regime at Daqiao deposit. This quantitative study emphasizes that the pressure-driven hydrothermal process plays a key role in the micron- to nano-scale redistribution and re-enrichment of gold and other trace metals during episodic replacement of auriferous pyrite in brittle rheological zones from epizonal orogenic gold systems.

Keywords: Replacement of pyrite; Marcasite overgrowth; Gold remobilization; fluid perturbation; Orogenic gold mineralization

## 1. INTRODUCTION

Dissolution and reprecipitation replacement of auriferous iron sulfides and sulfarsenides, typically pyrite ($FeS_2$, cubic), marcasite ($FeS_2$, orthorhombic), pyrrhotite ($Fe_{1-x}S$, x=0–0.125) and arsenopyrite (FeAsS), is ubiquitous in hypogene gold mineralization systems worldwide (e.g., Morey et al., 2008; Sung et al., 2009; Cook et al., 2013; Rottier et al., 2016; Fougerouse et al., 2016). Such replacement occurs when an externally-derived hydrothermal fluid comes into contact with pre-

existing auriferous sulfide and sulfarsenide minerals with which they are under-saturated. These minerals begin to dissolve and form an interfacial layer of fluids at the mineral surfaces that is supersaturated with respect to a more stable product phase (Putnis, 2002, 2009; Brugger et al., 2010; Qian et al., 2010, 2011; Harlov et al., 2011; Altree-Williams et al., 2015). Comprehensive studies of replacement of auriferous iron sulfides and sulfarsenides are therefore crucial to decipher redistribution and re-enrichment of gold (e.g., visible gold) plus other trace metals, and to monitor fluctuations in ore fluid fluxes and compositions, especially in the formation of giant and high-grade ore shoots (e.g., Tomkins and Mavrogenes, 2001; Tomkins et al., 2007; Morey et al., 2008; Cook et al., 2009, 2013; Sung et al., 2009; Thomas et al., 2011; Rottier et al., 2016; Fougerouse et al., 2016, 2017). However, the micron- to nano-scale textural diversity and complexity that arise from replacement may significantly obscure the original characteristics of auriferous mineral precipitation (Putnis, 2009; Altree-William et al., 2015), hampering a process-based interpretation for high grade gold ores evolution.

Previous studies of replacement of auriferous minerals in hydrothermal gold deposits mostly focus on pyrite-arsenopyrite and associated metal redistribution and reprecipitation (e.g., Dubé et al., 2004; Large et al., 2007; Morey et al., 2008; Cook et al., 2009, 2013; Sung et al., 2009; Fougerouse et al., 2016; Selvaraja et al., 2017; LaFlamme et al., 2018). However, the details of replacement behavior of marcasite, a polymorph of pyrite and a significant gold-hosting iron sulfide in many hydrothermal gold deposits (e.g., Arehart et al., 1993; Fleet and Mumin, 1997; Cline, 2001; Pals et

al., 2003; Franchini et al., 2015; Rottier et al., 2016), and related metal redistribution process has not been documented. Marcasite formation is kinetically favored over pyrite, but it is metastable in many geological environments and thus tends to be highly reactive. Formation and preservation conditions for marcasite have been experimentally documented, with stability favored at low pH and low temperature (Murowchick and Barnes 1986; Murowchick, 1992; Qian et al., 2011). Natural marcasite overgrowths on pre-existing pyrite have been described in a small number of low-temperature hydrothermal uranium deposits and sedimentary rocks (Goldhaber et al, 1978, 1979; Schieber and Riciputi, 2005; Schieber, 2007, 2011). In these cases, however, no specific formation mechanism was identified for the aggregates of pyrite and marcasite other than a "general replacement". Moreover, metal transfer related to these processes has not been quantitatively documented.

Despite the potential contribution of dissolution and reprecipitation reactions to the replacement of auriferous iron sulfides and sulfarsenides, the details of these processes and associated redistribution of gold are poorly understood, partly due to the very fine-grained size (less than a few tens of microns) of replacement minerals and ambiguous replacement textures. Previous studies of trace element redistribution during replacement processes have mostly relied on scanning electron microscopy-energy dispersive X-ray spectroscopy (SEM-EDS), electron microprobe (EMP) and laser ablation-inductively coupled plasma-mass spectrometry (LA-ICP-MS) (Fleet and Mumin, 1997; Morey et al., 2008; Cook et al., 2009, 2013; Sung et al., 2009). However, the utility of the SEM-EDS and EMP is limited because of the low

concentrations of trace elements relative to detection limits. Although LA-ICP-MS can provide quantitative results for trace elements present at very low concentrations (>0.01 ppm; Large et al., 2009), the spot size of laser beam is quite large (30–75 μm) relative to the details of micron- to nano-scale chemical variation. Ion probe mapping using NanoSIMS (Nanoscale secondary ion mass spectrometry) has the advantage of combined sub-50 nm lateral resolution and low detection limits and provides an attractive option for qualitative mapping of low concentrations of trace elements at high spatial resolution (McLoughlin et al., 2011). Furthermore, SIMS, with a spot size as small as 10 μm, provides an opportunity to study sulfur isotopic variation between the different generations of sulfides and their replacements (Chen et al., 2015).

In this study, we document details of textures and overprinting relationships for auriferous pyrite replaced by pyrite and marcasite in breccia gold ores from the Mesozoic Daqiao epizonal orogenic gold deposit, West Qinling Orogen, China. In-situ LA-ICP-MS trace element spot and line analyses and NanoSIMS element mapping combined with SIMS sulfur isotope analysis are used to reveal the redistribution of gold and other trace elements and related variations in sulfur isotopic composition. A mechanism to explain the observations is proposed, and implications for fluid-mediated pyrite replacement and related metal transfer in hydrothermal gold systems are discussed.

## 2. GEOLOGICAL BACKGROUND AND SAMPLING

The Qinling Orogen formed as a result of the prolonged subduction of the proto-

Tethyan ocean and subsequent collision between the North China Craton (NCC) and Qinling micro-plate along the Shangdan suture in the middle Paleozoic, and subduction of the paleo-Tethyan ocean and subsequent collision between the Qinling terrain and the South China Block (SCB) along the Mianlue suture in the Early Mesozoic (Fig. 1a; Meng and Zhang 1999; Dong et al. 2011). This orogen extends along a NW-strike for 2,500 km from the Dabie Mountains in the east to the Qilian Mountains and Kunlun Mountains in the west (insert of Fig. 1a). The West Qinling Orogen (WQO), separated from the East Qinling Orogen (EQO) broadly by the Baocheng Railway, can be further divided into the northern, central and southern domains by the Shangdan suture and Hezuo-Lintan-Liangdang Fault (HLLF), respectively (Wu et al., 2018a). The northern domain is an early Paleozoic oceanic arc, while the central and southern domains are characterized by greenschist-facies Devonian flysch metasedimentary rocks and unmetamorphosed to low-grade Triassic turbidites, respectively (Mao et al., 2002). The Triassic syn- to post-collisional granitoids (250–200 Ma) widely distribute in the WQO (Zeng et al., 2014).

The central and southern domains of the WQO host numerous orogenic gold deposits, which are thought to have formed during Late Triassic to Early Cretaceous peaking at ca. 216–200 Ma and 144–125 Ma (Wu et al., 2018b). Gold deposits are mostly localized along several crustal-scale, first-order southward thrust faults, such the HLLF and ZCHF (Zhouqu-Chengxian-Huixian-Fengxian Fault), which strike northwest to nearly east-west in excess of 400 km (Fig. 1a). These faults are thought to have formed during the Late Jurassic to Early Cretaceous north-south compression

in the Qinling orogenic belt (Dong et al., 2016). Seismic reflection profiling indicates that the overthrust belt is characterized by complex stacking thrust sheets, duplexes and opposed folds and faults (Liu et al., 2006). It is proposed that these crustal-scale thrust faults are channels for large-scale upwards-directed migration of fluids generated at depth (Robert et al., 1995).

The Daqiao orogenic gold deposit of latest Jurassic and Early Jurassic age in the southern domain has more than 105 t of gold resources at an average grade of 3–4 g/t (Wu et al., 2018a). The comprehensive deposit geology has been described in Wu et al. (2018a) and briefly summarized here. Orebodies are structurally controlled by a number of second-order reverse faults steeply dipping 55 to 80° north or southwest and mostly localized in fracture zones at the contact between Triassic turbidites and Carboniferous limestone (Fig. 1b). High-angle reverse faults are suggested to be fluid-activated valves that controlled flow from geopressured reservoirs, drove cyclic fluctuations in fluid pressure that caused mineral precipitation (e.g., Sibson et al., 1988; Cox, 1995; Robert et al., 1995).

Two economic styles of breccia, tectonic and hydraulic breccias, have been identified in the mine (Fig. 2). The strongly silicified tectonic breccia A contains disseminated auriferous pyrite and marcasite (up to 4 g/t; Fig. 2a and b). Tectonic breccias with high competence were hydraulically brecciated (Fig. 2c) and the resultant hydraulic breccia B is filled with chalcedony and irregular fine-grained cement-hosted pyrite, minor marcasite and arsenopyrite (Fig. 2d and e). Breccia B was further hydraulically brecciated to form more complex high-grade (up to 12 g/t)

breccia C cemented by calcite, pyrite, marcasite, and minor chalcedony (Fig. 2d and e).

A detailed interpretation of hydrothermal stages and different generations of sulfides is provided by Wu et al. (2018a). The early-ore stage sulfide euhedras and aggregates ($Py_2$, $Py_3$, $Py_4$, $Mc_1$, and $Mc_2$) are dominantly hosted by tectonic breccia A (Fig. 2a and b), whereas the main-ore stage sulfides ($Py_5$ and $Mc_3$) mainly occur in hydraulic breccias B and C (Fig. 2d and e). In the late-ore stage, non- or sub-economic coarse-grained marcasite and minor pyrite-pyrrhotite-calcite veins ($Py_6$ and $Mc_4$) developed in altered slates (Fig. 2f).

Complex early- to main-ore stage aggregates of various generations of pyrite and marcasite occur in the breccias in both the tectonic and hydraulic breccia ores at Daqiao deposit. Approximately fifty unweathered breccia (A, B, and C) samples were collected from outcrops, open pits, boreholes, and underground tunnels in order to provide a representative suite of samples for petrographical and geochemical analyses (Fig. 1b).

## 3. METHODS

Samples containing iron sulfides, and typical host rocks, were prepared as polished thick and thin sections. The thick sections were examined under optical microscopy to characterize the multiple generations of sulfides, and areas of interest (3–5 mm in diameter) were drilled out and mounted in 25-mm diameter epoxy discs together with pyrite standards for SIMS sulfur isotope analysis (Chen et al., 2015).

198 The samples were carefully polished, sonicated, and mount-scale photomicrographed
199 under an optical microscope using reflected light. The images were used to navigate
200 to regions of interest to perform the microanalyses. Prior to in-situ compositional and
201 sulfur isotopic analyses, the polished discs were carbon coated and imaged with the
202 scanning electron microscope (SEM) in backscattered electron (BSE) and secondary
203 electron (SE) modes to determine the detailed mineralogy, qualitative mineral
204 compositional zoning, textural relationships and paragenesis. We used a diverse
205 combination of micro-analytical techniques to investigate the elemental and isotopic
206 characteristics of various generations of pyrite and marcasite. The methodology is
207 summarized below and more standard and specific details for each are given in
208 Appendix A.

209 **3.1. LA-ICP-MS multi-element analysis of sulfides**

210 Concentrations of trace elements in pyrite and marcasite were determined using
211 laser-ablation inductively coupled plasma-mass spectrometry (LA-ICP-MS) at
212 CODES, University of Tasmania. This instrumentation employs a New Wave 213-nm
213 solid-state laser microprobe coupled to an Agilent 4500 quadrupole ICP-MS. The
214 method is described in detail in Large et al. (2009) and Thomas et al. (2011). Spot
215 ablation was carried out using a 25 to 40 micrometer spot size at 5 J/cm$^2$ and using 5
216 Hz, with a 30 s baseline and 30–45 s of ablation. Two laser profiles with profile
217 lengths of 500 to 600 μm across pyrite and marcasite aggregates were also measured.
218 Thirty-nine LA-ICP-MS spot analyses on pyrite and thirty-three on marcasite were
219 measured (Table B.1).

### 3.2. NanoSIMS multi-element imaging of sulfides

After trace element analysis, the epoxy mounts were polished with a series of diamond polishing powders (down to 1 μm) to minimize surface topography and coated with 10 nm of platinum to provide conductivity at high voltage. NanoSIMS analysis was performed at the Centre for Microscopy, Characterisation and Analysis (CMCA) at the University of Western Australia (UWA), using a CAMECA NanoSIMS 50L. The method is described in McLoughlin et al. (2011). A $Cs^+$ ion source with a spot size of approximately 50 nm was employed. Negative secondary ions ($^{34}S^-$, $^{63}Cu^{32}S^-$, $^{60}Ni^{32}S^-$, $^{75}As^{32}S^-$, $^{123}Sb^-$, and $^{197}Au^-$) were then sputtered from the sample surface using a beam current of ~2.5 pA.

### 3.3. SIMS sulfur isotope analysis

High-precision secondary ion mass spectrometry (SIMS) S-isotope analysis was carried out using the Cameca IMS-1280 at the Institute of Geology and Geophysics (Beijing), Chinese Academy of Sciences. Analytical conditions and procedures for high-precision S-isotope analyses with this IMS-1280 are described in detail elsewhere (Chen et al., 2015). We used the same parameters as Chen et al. (2015) and applied a $Cs^+$ primary ion beam, with a spot size of approximately ~10×15 μm, impact energy of 10 kV, and an intensity of ~2.5 nA.

Analyses of matrix-matched reference material should be used to correct the mass fractionation during SIMS analysis (e.g., LaFlamme et al., 2016, 2018). However, due

to a lack of suitable marcasite standard, two pyrite standards: Sonora pyrite ($\delta^{34}S_{VCDT}$ = +1.61‰; Farquhar et al., 2013) and Balmat pyrite ($\delta^{34}S_{VCDT}$ = +16.12 ± 0.68‰, 2 $\sigma$; Whitehouse, 2013) were used during both the pyrite and marcasite analysis sessions. Pyrite standard has been utilized for SIMS and LA-MC-ICP-MS sulfur isotope analysis for marcasite in other studies (e.g., Rouxel et al., 2008; Wong et al., 2017). Here, we use a comparison of results from the two techniques to assess potential matrix effects. Eighteen SIMS spot analyses on pyrite and twenty-nine on marcasite were measured (Table B.2).

# 4. RESULTS

## 4.1. Petrographic features

Detailed optical and SEM petrographic observations revealed that inclusion-free pyrite is surrounded by porous pyrite, that is, in turn, bordered by marcasite together with minor arsenopyrite in the Daqiao breccias (Fig. 3, Table 1). Sulfide generations and replacement/overgrowth reactions are described with notation of the form $X_{i\text{-}j}$, which means that sulfide X of generation i is inferred to have replaced and/or overgrown sulfide j of a previous generation. The generations of interest here are $Py_3$, $Py_{4\text{-}py}$, $Mc_{2\text{-}py}$ in the early-ore stage, and $Mc_{3\text{-}py}$ and Apy in the main-ore stage.

$Py_3$ aggregates (0.01–2 mm across) are generally nonporous and free or almost free of mineral inclusions (Fig. 3a-g). Py3 commonly contains narrow internal cyclic elemental zones in the SEM images (Fig. 3c and d).

$Py_{4\text{-}py}$ (0.01–1 mm across) borders $Py_3$ (Fig. 3a-d) and is also present in $Py_3$

265 microfractures and interstitial spaces between $Py_3$ grains (Fig. 3e-g and i). $Py_{4\text{-}py}$
266 commonly contains mineral inclusions (5–100 μm in diameter), such as chalcopyrite,
267 galena, and arsenopyrite (Fig. 3a-c, and e). $Py_{4\text{-}py}$ aggregates are characterized by
268 abundant pores varying in size (1–50 μm in diameter), which exhibit no perceptible
269 preferred orientation. Porosity in most of $Py_{4\text{-}py}$ occupies approximately 1–10 %, or in
270 some cases 10–25 % of the volume, although we note that the petrographical
271 techniques used are not quantitative and cannot identify sub-micron pores. The
272 contact between $Py_3$ and $Py_{4\text{-}py}$ is sharp and curvilinear (contact marked with yellow
273 lines in Fig. 3a-g, i and k).

274 Marcasite consisting of $Mc_{2\text{-}py}$ and $Mc_{3\text{-}py}$ is anisotropic with yellowish-brown to
275 grayish-blue polarization colors (Fig. 3e-h and k). $Mc_{2\text{-}py}$ and $Mc_{3\text{-}py}$ are commonly
276 intergrown and are characterized by a bimodal grain size distribution with a fine (1–
277 100 μm) and a coarse (up to 300 μm) grained domain (Fig. 3k and l). In the fine-
278 grained domains, $Mc_{2\text{-}py}$ microcrystals occurs as aggregates surrounding $Py_{4\text{-}py}$, with
279 sharp, planar to curvilinear interfaces between $Py_{4\text{-}py}$ and $Mc_{2\text{-}py}$ (contact marked with
280 red lines in Fig. 3e-l). Porous $Mc_{2\text{-}py}$ and $Mc_{3\text{-}py}$ also contains irregular $Py_{4\text{-}py}$
281 inclusions and shows similar external morphology with euhedral $Py_{4\text{-}py}$ grains (Fig. 3g
282 and h). $Mc_{2\text{-}py}$ commonly displays some fine pores and a lower average atomic mass
283 than $Py_{4\text{-}py}$ shown as a darker color in BSE images (Fig. 3i and j). Zoned $Mc_{3\text{-}py}$, in
284 some cases, surrounds $Mc_{2\text{-}py}$ crystals and varies in size (1–10 μm; Fig. 3l). In BSE
285 image of the fine-grained domains, marcasite aggregates are zoned with irregular
286 bright, sector and sub-micrometer cyclic bands of $Mc_{3\text{-}py}$ in $Mc_{2\text{-}py}$ crystals (Fig. 3m),

suggesting a precipitation cyclicity between $Mc_{2\text{-}py}$ and $Mc_{3\text{-}py}$. There are minor fine-grained Apy veinlets or inclusions (1–10 μm), closely intergrown with $Mc_{2\text{-}py}$ and zoned $Mc_{3\text{-}py}$ (Fig. 3i, j and l).

The coarse-grained domains generally border the fine-grained $Mc_{2\text{-}py}$ and $Mc_{3\text{-}py}$ domains (contact marked by white lines in Fig. 3k and l). In this domain, tabular $Mc_{2\text{-}py}$ contains little porosity. Infrequent sub-micron $Mc_{3\text{-}py}$ bands are present in $Mc_{2\text{-}py}$, and Apy inclusions are notably absent (Fig. 3l).

### 4.2. Sulfide trace element compositions

Wu et al. (2018a) report LA-ICP-MS spot analyses of all the different generations of pyrite and marcasite from the Daqiao deposit, and interpret these data in the context of sulfide evolution and deposition mechanisms during hydrothermal fluid flow and gold mineralization. In this study, we present additional LA-ICP-MS data that enable a better understanding in the complex textures of pyrite and marcasite aggregates in the breccias. Seventy-two previously unreported analyses of pyrite and marcasite given in Table B.1 are summarized in Table 2. The results (Fig. 4) are based on combination of the 72 spot analyses and the data reported in Wu et al. (2018a). Data from two previously unreported LA-ICP-MS transects across complex sulfide aggregates are also presented in Figure 5. Because of the large compositional variations, median values are used for comparison (Fig. 6).

*$Py_3$*

Gold contents in the euhedral inclusion-free $Py_3$ interpreted as early-ore stage vary

from b.d.l. (below detection limit) to 107 ppm with a median of 0.5 ppm, while arsenic ranges from b.d.l. to 87444 ppm (median = 3115 ppm, *n* = 49; Fig. 4a). A range of other trace elements occurred at concentrations above the detection limits in $Py_3$, mainly including Co, Ni, Cu, Zn, Se, Ag, Sb, Tl, and Pb (Table 2, Fig. 4b-f). Spikes in As, Co, Ni, Sb, Cu, and Tl were revealed by the LA-ICP-MS line analyses (Fig. 5c and d).

*$Py_{4\text{-}py}$*

Based on results of thirty-three LA-ICP-MS spot analysis, trace elements in $Py_{4\text{-}py}$ can be classified into two groups that are enriched and depleted in comparison to $Py_3$ (Figs. 4-6). The enriched group consists of Cu, Sb, Ag, Pb, and Bi. The depleted group includes Au (median = 0.09 ppm), As (median = 130 ppm), Te, Se, Zn, Co, Tl, Ni, and W (Fig. 6a). Some $Py_{4\text{-}py}$ domains show spikes of As, Cu, Sb and Tl in the LA-ICP-MS laser profiles (Fig. 5c and d).

*$Mc_{2\text{-}py}$*

Forty-four spot analyses of $Mc_{2\text{-}py}$ reveal that a small number of trace elements are enriched in $Mc_{2\text{-}py}$ relative to $Py_3$ (Figs. 4 and 6a). These elements include Sb, Ag, Zn, and W. Concentrations of other trace elements are much lower than those both in $Py_3$ and $Py_{4\text{-}py}$, notably for Au (median = 0.08 ppm), As (median = 21 ppm), Co, Ni, Pb, and Bi. In the laser profiles, it was difficult to obtain trace element contents of unmixed $Mc_{2\text{-}py}$ or $Mc_{3\text{-}py}$ because the spot size of laser beam was larger relative to the zone width (Fig. 5c and d).

*$Mc_{3\text{-}py}$*

The main-ore stage $Mc_{3\text{-}py}$, which occurs in irregular zones with higher average atomic mass than early-ore $Mc_{2\text{-}py}$, shown in brighter BSE images (Fig. 3l and m) is enriched in a suite of trace elements relative to $Py_3$, $Py_{4\text{-}py}$ and $Mc_{2\text{-}py}$ (Figs. 4-6). Based on the results of forty spot analyses, elements enriched in $Mc_{3\text{-}py}$ compared to $Py_3$ and $Py_{4\text{-}py}$ are Au (median = 5.8 ppm), W, Tl, Ag, Sb, Se, and Zn. Elements depleted in $Mc_{3\text{-}py}$ relative to $Py_3$ and $Py_{4\text{-}py}$ include Te, Ni, Co and Bi. Although As is depleted in $Mc_{3\text{-}py}$ (median = 2578 ppm ppm) relative to $Py_3$, it is higher in $Mc_{3\text{-}py}$ than in $Py_{4\text{-}py}$ (Fig. 6).

The LA-ICP-MS ablation profiles clearly reveal 2–3 distinctive spikes that record zones in the $Mc_{2\text{-}py}$–$Mc_{3\text{-}py}$ aggregates that are enriched in As, Sb, Tl, Cu, and minor Au (marked with red arrows on Fig. 5c and d). Relative trace element concentrations in the two generations of marcasite ($Mc_{2\text{-}py}$ and $Mc_{3\text{-}py}$) are more similar to each other than they are to $Py_3$, in spite of higher absolute trace element concentrations in the zones of $Mc_{3\text{-}py}$ (Fig. 6).

*Apy*

Fine Apy grains or veinlets mainly occur as 1–10 μm intergrowths with zoned $Mc_{3\text{-}py}$ (Fig. 3i, j and l). The size of the Apy is smaller than the laser beam, so it was not possible to obtain unmixed analyses of Apy. A small number of SEM-EDS analyses of the Apy grains were obtained (not shown), and these fall on a compositional mixing line between $FeS_2$ and FeAsS, indicating the analyses are Apy-$Mc_{3\text{-}py}$ mixtures, or that the Apy is depleted in As.

### 4.3. Trace element distribution in sulfides

A typical sulfide texture involving co-existing $Py_3$, $Py_{4\text{-}py}$ and marcasite was chosen for NanoSIMS mapping (boxed area on Fig. 7a). The high-resolution NanoSIMS images reveal three chemical microbands in $Py_3$ (~0.5 μm across; marked with red arrows; Fig. 7c-g). These bands are of continuous shape and are enriched in Ni, As, and Sb, and to a less extent, Au and Cu compared to the host $Py_3$. These metal-rich microbands are compositionally consistent with the chemical zoning recorded in the LA-ICP-MS line analyses across $Py_3$ (Fig. 5c and d).

The micropores in the $Py_{4\text{-}py}$ and $Mc_{2\text{-}py}$ appear dark in the NanoSIMS elemental maps (Fig. 7b). Arsenic, Sb, and Au are heterogeneously distributed in porous $Py_{4\text{-}py}$. Cu enrichment occurs as inclusions (0.25–1 μm across; marked with green arrows) in $Py_{4\text{-}py}$ and $Mc_{3\text{-}py}$ (Fig. 7c). Euhedral or irregular $Mc_{2\text{-}py}$ has lower Cu and Ni concentrations than $Py_3$ while As, Sb, and Au contents are elevated in $Mc_{2\text{-}py}$ relative to $Py_3$ though this may be due to some extent to a partial contribution from $Mc_{3\text{-}py}$. The $Mc_{3\text{-}py}$ zones (1–3 μm in thickness) and minor Apy aggregates are characterized by depletion of $^{34}S$ compared to $Py_3$, $Py_{4\text{-}py}$, and $Mc_{2\text{-}py}$ (Fig. 7b). The highest As, Sb, and Au concentrations are associated with irregular finger shaped zones of $Mc_{3\text{-}py}$ (Fig. 7e-g), which are characterized by a higher average atomic mass than $Py_3$, $Py_{4\text{-}py}$, and $Mc_{2\text{-}py}$ in the BSE images (Fig. 7a). There is no Ni enrichment in $Py_{4\text{-}py}$, $Mc_{2\text{-}py}$ or $Mc_{3\text{-}py}$ (Fig. 7d).

In the NanoSIMS line profile (Fig. 7h), five zones with elevated Cu, As, Sb and Au ion counts (concentrations) can be identified in $Py_3$. The $Mc_{3\text{-}py}$ and Apy

aggregates also display zoning; three peaks exhibit high concentrations of trace elements compared to other immediately adjacent iron sulfides (Fig. 7h). The three peaks in $Mc_{3\text{-}py}$ correlate with regions of $^{34}S$ depletion; however, similar peaks in $Py_3$ are not associated with sulfur isotopic variations.

### 4.4. Sulfur isotopes

The sulfur isotopic compositions presented herein are from high-resolution, previously unpublished SIMS analyses (Fig. 8, Table B.2). The $\delta^{34}S$ values of a total of thirteen analyses of $Py_3$ vary from +1.9 to +9.0‰, with a mean of +4.6‰ ($\sigma$ = 1.9); five analyses of $Py_{4\text{-}py}$ vary from +1.7 to +4.3‰, with a mean of +2.9‰ ($\sigma$ = 1.0); thirteen analyses of $Mc_{2\text{-}py}$ vary from -0.9 to +3.7‰, with a mean of +2.4‰ ($\sigma$ = 1.2); sixteen analyses of $Mc_{3\text{-}py}$ yield a large range in $\delta^{34}S$ value from -11.4 to +2.2‰ (mean -1.3‰, $\sigma$ = 4.4). In contrast, the mean LA-MC-ICP-MS sulfur isotopes of these four types of sulfides ($Py_3$, $Py_{4\text{-}py}$, $Mc_{2\text{-}py}$, and $Mc_{3\text{-}py}$) are +5.2‰ (s.d. = 2.4, n = 17), +3.4‰ (s.d. = 1.3, n = 11), +5.0‰ (s.d. = 3.9, n = 17), and -9.7‰ (s.d. = 6.2, n = 6), respectively (Fig. 8, Wu et al., 2018a).

## 5. DISCUSSION

### 5.1. Textual interpretations

#### *5.1.1. Pyrite replacement by pyrite*

Detailed textural observations demonstrate that porous $Py_{4\text{-}py}$, together with chalcopyrite, galena and arsenopyrite inclusions, occurs preferentially along micro-fractures and grain margins of $Py_3$ (Fig. 3). The reaction front is sharp and curvilinear

at sub-micron resolution of the NanoSIMS mapping and profile (Fig. 7). These observations are taken as evidence supporting the idea that $Py_{4\text{-}py}$ mainly formed by replacement of $Py_3$ via a dissolution and reprecipitation mechanism (Table 1). Preservation of some aspects of the external morphology of parent $Py_3$ (Fig. 3a-d) implies some degree of a spatial and temporal coupling between the dissolution and reprecipitation (cf. Putnis, 2002, 2009; Altree-Williams et al., 2015). However, it is still possible that some $Py_{4\text{-}py}$ overgrowth may coarsen the external dimension of parent $Py_3$ that was replaced by $Py_{4\text{-}py}$.

The volume reduction necessary to create the observed porosity in product $Py_{4\text{-}py}$ may be accommodated by some combination of a lower molar volume relative to $Py_3$, and the partial dissolution of parent $Py_3$ into the fluid (Walker et al., 1995; Putnis, 2002, 2009; Rubatto et al., 2008). It has been calculated that pyrite containing 3.8 wt% arsenic ($Fe_{32}S_{62}As_2$) has an expansion of 0.83 % in volume relative to pure pyrite as a consequence of the greater length of As-S bonds than S-S bonds (Blanchard et al., 2007). During the replacement of arsenic-rich $Py_3$ by arsenic-depleted $Py_{4\text{-}py}$ (median 3115 ppm vs. 130 ppm As), the As-induced volume decrease alone cannot explain the 1–10 vol% porosity in $Py_{4\text{-}py}$ (Fig. 3). Volume reduction during hydrothermal replacement has been suggested to be due to dissolution of parent phase in excess of the product phase precipitated, because of their different solubilities in the interfacial fluids (Putnis, 2002, 2009). However, in this case of pyrite replacement by pyrite, the solubility is not expected to change much.

It has also been suggested that porosity in pyrite from hydrothermal gold deposits

420 is a consequence of rapid crystallization (Simon et al., 1999). Porous pyrite formed
421 via rapid growth is characterized by aggregates of fine grain size microcrystals,
422 several microns across, with the grain size distribution controlled by rapid nucleation
423 relative to crystal growth (Butler and Richard, 2000). Concentrations of Au, As (e.g.,
424 up to 2.4 wt% As and 1600 ppm Au; Simon et al., 1999), and other trace elements are
425 high because the extra vacancies and surface defects associated with rapid growth
426 facilitate their incorporation (Reich et al., 2005). Aggregates of porous $Py_{4\text{-}py}$ at
427 Daqiao deposit contains much lower contents of Au, As and other trace metals (130
428 ppm As and 0.1 ppm Au; Fig. 4) than $Py_3$. However, this compositional difference
429 does not eliminate a rapid growth, since trace element concentrations around could be
430 low during the $Py_{4\text{-}py}$ reprecipitation.
431
432 *5.1.2. Marcasite relationships*
433 Aggregates of $Mc_{2\text{-}py}$ and $Mc_{3\text{-}py}$ commonly occur on the margins of $Py_{4\text{-}py}$ (Fig.
434 3e, f, i, k and l), or as euhedral grains containing irregular $Py_{4\text{-}py}$ inclusions (Fig. 3g
435 and h). Several lines of textural evidence, including the sharp, planar to curvilinear
436 interface between $Py_{4\text{-}py}$ and $Mc_{2\text{-}py}$ (Fig. 3e-l), fine pores in $Mc_{2\text{-}py}$ (Fig. 3e-l), some
437 degree of preservation of $Py_{4\text{-}py}$ external dimension (Fig. 3g and h), and occurrence of
438 fine-grained Apy inclusions with $Mc_{2\text{-}py}$ and $Mc_{3\text{-}py}$ (Fig. 3i, j and l), imply that $Mc_{2\text{-}py}$
439 and $Mc_{3\text{-}py}$ aggregates probably formed by replacement of $Py_{4\text{-}py}$ (Table 1). However,
440 during the replacement of $Py_{4\text{-}py}$, cyclic precipitation between $Mc_{2\text{-}py}$ and zoned $Mc_{3\text{-}py}$
441 (Fig. 3m) indicates that there may have been switching between the early-ore and
442 main-ore conditions as the ore-forming process progressed.

In some cases, aggregates of fine-grained $Mc_{2\text{-}py}$ crystals and zoned $Mc_{3\text{-}py}$ with little porosity formed directly on $Py_{4\text{-}py}$ margins where this is no sign of dissolution (Fig. 3l). This texture implies that the marcasite reprecipitation is not tightly coupled with dissolution of $Py_{4\text{-}py}$ (Putnis, 2009; Xia et al., 2009). The degree of coupling between dissolution and precipitation is thought to be controlled by fluid parameters, such as pH, and the degree of supersaturation (Xia et al., 2009; Qian et al., 2011).

Experimental studies have demonstrated that pyrite with fine, homogenous porosity intergrown with marcasite can form via solid-state marcasite transformation in a closed system at temperatures of 425–500 °C (Table 1, Fleet, 1970; Murowchick, 1992). However, the observed 1–50 μm pores (1–10 vol%) in $Py_{4\text{-}py}$ are quite different to those in pyrite produced in the experiment. Moreover, it has been suggested that the rate of solid-state reaction is relatively slow in sulfides even at high temperatures. For example, iron sulfides with peak metamorphic temperature of 500–600 $^{o}$C preserve Co and sulfur isotope zoning on the micron scale (Evans et al., 2014). Kinetic studies suggest that a half-life for the solid-state transformation of marcasite to pyrite at 200 °C is $3\times10^{6}$ yr (Lennie and Vaughan, 1992). Precipitation of pyrite and marcasite or their aggregates can occur on timescales of only a few hours under hydrothermal conditions and temperatures to 220 °C (Qian et al., 2011). At Daqiao deposit, conditions were fluid-rich (Wu et al., 2018a) and temperatures are thought to have been low (ca. 100–240 °C; Xu et al., 2015), within the stability field of marcasite (temperature less than 240°C; Murowchick and Barnes, 1986). It is therefore likely that solid-state transformation was not a significant contributor to replacement of

pyrite by marcasite.

Coarse-grained $Mc_{2\text{-}py}$ domains also occur perpendicular to aggregates of $Mc_{2\text{-}py}$ and $Mc_{3\text{-}py}$ (Fig. 3k and l). These $Mc_{2\text{-}py}$ euhedra contain few pores in comparison to those in $Mc_{2\text{-}py}$ inferred to have formed by replacement of porous $Py_{4\text{-}py}$. Cementation of $Mc_{2\text{-}py}$ idiomorphic crystals indicates that marcasite precipitated from fluids as new grains or as overgrowths rather than forming during pyrite replacement (cf. Zhao et al., 2014). In summary, $Py_3$ was replaced first by porous $Py_{4\text{-}py}$, and the $Py_{4\text{-}py}$ was replaced by a combination of $Mc_{2\text{-}py}$, $Mc_{3\text{-}py}$ and minor Apy, then followed by overgrowth of coarse-grained $Mc_{2\text{-}py}$.

*5.1.3. Comparison with pyrite replacements reported in the literature*

Replacement of inclusion-free pyrite by porous, inclusion-rich pyrite has been reported from other hydrothermal systems (e.g., Su et al., 2008; Morey et al., 2008; Sung et al., 2009; Pal et al., 2011; Gao et al., 2017; Chen et al., 2018; Li et al., 2018). For example, porous rims of pyrite closely associated with visible gold have been suggested to form via hydrothermal alteration of pre-existing pyrite during increases in temperature and sulfur fugacity during prograde metamorphism (Morey et al., 2008). Porous As-poor pyrite with numerous arsenopyrite inclusions, documented at an Archean orogenic gold deposit, Western Australia, has been proposed to form by partial replacement of As-rich pyrite via fluid-mediated coupled dissolution and reprecipitation (Sung et al., 2009). This replacement of one phase by a porous variant of the same phase has also been observed for other minerals. For instance, the margins of Ni-bearing arsenopyrite from an Archean orogenic gold deposit have been reported

to be hydrothermally replaced by Ni-poor, native Au-bearing rims via dissolution and reprecipitation, with consequent Ni and Au remobilization (LaFlamme et al., 2018). Magnetite is widely hydrothermally replaced by porous, trace element-poor magnetite via the dissolution and reprecipitation (Wen et al., 2017). Magmatic zircon can be also replaced by porous secondary zircon carrying lower concentrations of trace elements than the precursor mineral, with replacement inferred to have occurred via aqueous fluid or melt-mediated coupled dissolution and reprecipitation (Geisler et al., 2007).

Partial dissolution of pyrite, associated with subsequent marcasite precipitation, has been documented in the low-temperature sandstone-hosted uranium deposits, U.S. (Goldhaber et al., 1979; Reynolds et al., 1982). In the global black shale successions ranging in age from Middle Proterozoic to Cretaceous, intermittent marcasite precipitation has also been interpreted to be initiated by oxidation and dissolution of the already existing sedimentary pyrite (Schieber and Riciputi, 2005; Schieber, 2007, 2011).

### 5.2. Trace element remobilization and gold re-enrichment

The LA-ICP-MS and NanoSIMS analyses highlight systematic trace element variations between the different generations of pyrite and marcasite (Figs. 4-7). In replacement of $Py_3$ by porous $Py_{4\text{-}py}$ (Fig. 6a), elements enriched in $Py_{4\text{-}py}$ relative to $Py_3$ (Cu, Sb, Ag, Pb, and Bi) may be sourced from infiltrating fluids, or from metals hosted in sub-micron inclusions (e.g., chalcopyrite, galena, arsenopyrite) formed during remobilization from $Py_3$. Existence of these fine mineral inclusions in porous

$Py_{4\text{-}py}$ is supported by the spikes of Cu and Sb in LA-ICP-MS laser profiles (Fig. 5c and d), as well as Cu nano-inclusions in NanoSIMS image (Fig. 7c). The presence of Cu, Pb, Ag, and Bi-bearing minerals in porous alteration pyrite-arsenopyrite assemblages formed via trace element remobilization and re-enrichment during hydrothermal replacement have been documented in other gold deposits (e.g., Morey et al., 2008; Sung et al., 2009; Cook et al., 2013). In contrast, metals (Te, Se, Zn, Co, Tl, Ni, Au, W, and As; Fig. 6a) depleted in porous $Py_{4\text{-}py}$ relative to $Py_3$, commonly exhibit zonation patterns in the parent $Py_3$ at Daqiao deposit (Figs. 5c, d and 7). Similar zonation for Au, As, Co, Ni, and Se in pyrite have also been reported from other hydrothermal gold ores (e.g., Cook et al., 2013; Yan et al., 2018). These metals that are depleted in porous $Py_{4\text{-}py}$ may have been expelled from the system during replacement of $Py_3$.

The trace element redistribution process during replacement of $Py_3$ by $Py_{4\text{-}py}$ plus minor inclusions (Ccp, Gn, Apy) may therefore be described by:

$$Py_3 + \text{fluids } (Cu^{2+}, Sb^{-}, Ag^{+}, Pb^{2+}, Bi^{2+})_{(aq)} \rightarrow Py_{4\text{-}py} + Ccp + Gn + Apy + \text{fluids } (Te^{-}, Se^{-}, Zn^{2+}, Co^{2+}, Tl^{1+}, Ni^{2+}, Au^{+}, W^{6+}, As^{-})_{(aq)} \quad (1)$$

Few previous studies have documented the compatibility of trace elements in marcasite relative to pyrite, so the processes that controlled trace element incorporation into product marcasite are difficult to determine. However, the solubility of most metals increases as pH decreases so the presence of fluids sufficiently acidic to stabilize marcasite (e.g., pH<2.5 at 220 $^{o}$C; Qian et al., 2011)

may have led to increased metal mobility and decreased metal compatibility (Reed and Palandri, 2006). Only W is notably enriched in both product $Mc_{2\text{-}py}$ and $Mc_{3\text{-}py}$ compared to the precursor $Py_{4\text{-}py}$. Tungsten is suggested to be transported mainly as carbonate or bicarbonate complexes in carbonic metamorphic fluids (Higgins, 1980), so fluid boiling-related decrease of $CO_2$ partial pressure could have resulted in W sequestration into marcasite. Other lines of evidence at Daqiao deposit, including the hydrothermally altered in-situ carbonaceous materials in breccia ores, and Au-rich fine-grained pyrite and marcasite characterized by negative $\delta^{34}S$ values hosted in hydrothermal cements, are also consistent with rapid fluid phase separation of a $CO_2$-bearing fluid phase, triggered by hydraulic fracturing (Wu et al., 2018a).

Despite the likely pH-induced decreased metal compatibility during marcasite precipitation, complex-zoned $Mc_{3\text{-}py}$ is enriched in a suite of trace elements compared to $Py_{4\text{-}py}$ (Fig. 6b). It has been suggested that metal-rich zones form due to a build-up of high trace element concentrations at local mineral-fluid interfacial layers (Putnis et al., 1995; Putnis and Mauthe, 2001). At the Daqiao deposit, this could manifest as rapid deposition of narrow $Mc_{3\text{-}py}$ zones together with fine-grained arsenopyrite on porous $Py_{4\text{-}py}$ (Figs. 3l and 7). Precipitation of $Mc_{3\text{-}py}$ could be initiated by a reduction in threshold of the supersaturation of metals near the interfacial layers triggered by changes in fluid chemistry. Metal enrichment in $Mc_{3\text{-}py}$ relative to $Py_{4\text{-}py}$ (W, Tl, Au, As, Sb, Ag, Se, and Zn; Fig. 6b) might have been derived to some combination of the $Py_{4\text{-}py}$ dissolution, and metals sourced from infiltrating fluids.

Trace element redistribution during replacement of $Py_{4\text{-}py}$ by $Mc_{2\text{-}py}$, $Mc_{3\text{-}py}$ and

554 minor Apy is described as:

555 $Py_{4\text{-}py}$ + fluids ($W^{6+}$, $Tl^{1+}$, $Au^{+}$, $As^{-}$, $Sb^{-}$, $Ag^{+}$, $Se^{-}$, $Zn^{2+}$,)$_{(aq)}$

556 $\rightarrow Mc_{2\text{-}py}$ + $Mc_{3\text{-}py}$ + Apy + fluids ($Cu^{2+}$, $Te^{-}$, $Pb^{2+}$, $Ni^{2+}$, $Co^{2+}$, $Bi^{+}$)$_{(aq)}$ (2)

557 It is interesting to note that trace elements enriched in $Py_{4\text{-}py}$ commonly occur as
558 an isovalent substitution for $Fe^{2+}$ in pyrite (e.g., Cu and Pb), while those depleted in
559 $Py_{4\text{-}py}$ relative to $Py_3$ either isovalently substitute for $S^{-}$ (Te, Se, and As; Deditius et al.,
560 2008) or $Fe^{2+}$ with potential As involvement (Co and Ni; Yang and Downs, 2008).
561 Trace elements such as Au, Ag, Tl, and Bi, which show coupled heterovalent
562 substitution for $Fe^{2+}$ with or without As, can display either relative enrichment (Ag
563 and Bi) or depletion (Tl and Au) in $Py_{4\text{-}py}$ compared to $Py_3$ (Eq. 1 – Fig. 6a). In
564 contrast, trace elements enriched (e.g., Se, Sb, and As) and depleted (Cu, Pb, Bi, Co,
565 and Ni) in the product zoned $Mc_{3\text{-}py}$ generally isovalently or heterovalently substitute
566 for $S^{-}$ and $Fe^{2+}$ in marcasite, respectively (Eq. 2 – Fig. 6b).

567 Little is known about the potential relations between metal redistribution patterns
568 in the replacement pyrite and marcasite and their elemental substitution mechanisms
569 during replacement via dissolution and reprecipitation reactions. It has been suggested
570 that mineral surfaces could become charged during chemical reactions at mineral-
571 solution interfaces (Stumm and Morgan, 1996). To reach electroneutrality between the
572 mineral surface and solution, the charged surfaces attract ions of opposite charge and
573 repels ions of similar charge (Smith, 1999). It is interesting to speculate if, to some
574 extent, metal enrichment generally related to $Fe^{2+}$ and $S^{-}$ substitutions in product
575 pyrite ($Py_{4\text{-}py}$) and marcasite ($Mc_{3\text{-}py}$), respectively, were associated with the different

charged reaction interfaces formed during the fluid-mediated replacement process. Changes in surface charge of iron sulfides has been suggested to be related to the changing pH in fluids (Widler and Seward, 2002; Qian et al., 2011).

### 5.3. Drivers for replacement and overgrowth

#### *5.3.1. Pyrite replaced by pyrite*

When one phase is replaced by the same phase with a new composition, the substituted solid solutions in the parent phase tend to exsolve to reduce the strain energy, which enhances the surface reactivity and thus the dissolution rate (Geisler et al., 2007). Non-stoichiometric parent phases are likely have higher solubility in fluid than ideal stoichiometric end-member of the daughter phase, which drives dissolution and reprecipitation (Lippmann, 1980; Fougerouse et al., 2016). In addition, it has been proposed that arsenic enrichment in the pyrite lattice can effectively accelerate fluid-mediated pyrite dissolution since the formation of sulfur vacancies preferentially proceeds in the vicinity of arsenic (Blanchard et al., 2007). LA-ICP-MS trace element analysis reveals the much higher contents of As (median 3115 ppm vs. 130 ppm As; Fig. 4a) plus other solid solutions (Te, Se, Zn, Co, Tl, Ni, Au, W, and As; Fig. 6a) in parent $Py_3$ than product $Py_{4\text{-}py}$. These high impurity concentrations provide a driver for replacement of $Py_3$ by $Py_{4\text{-}py}$ during fluid infiltration.

#### *5.3.2. Pyrite replaced by marcasite*

It has been proposed that pyrite replacement textures and subsequent marcasite precipitation in sandstone-hosted uranium deposits and black shales result from

599 oxidation and dissolution of pre-existing pyrite (e.g., Granger and Warren, 1974;
600 Goldhaber et al., 1978, 1979; Reynolds et al., 1982; Schieber and Riciputi, 2005;
601 Schieber, 2007, 2011). These reactions have been suggested to proceed mainly via
602 Eqs. 4 – 7 (Goldhaber et al., 1978; Schieber, 2007):

603 $FeS_{2\ (pyrite)} + 3.5\ O_2 + H_2O = Fe^{2+} + 2H^+ + 2SO_4^{2-}$ (4)

604 $2FeS_{2\ (pyrite)} + 3.5\ O_2 + 3H_2O = 2FeO\ (OH) + 4H^+ + 4S_2O_3^{2-}$ (5)

605 $nH^+ + nS_2O_3^{2-} + 2H_2S_{\ (aq)} = 2H_2S_n + nHSO_3^-$ (6)

606 $Fe^{2+} + H_2S_n = FeS_{2\ (marcasite)} + S_{n-2}{}^0 + 2H^+$ (7)

607 Experimental studies have demonstrated that marcasite precipitation is strongly
608 favored over pyrite at $pH<pK_1$ of the aqueous polysulfide species present (e.g., for
609 $H_2S_2$, $pK_1 = 5$, at 25°C; Murowchick and Barnes, 1986; Schoonen and Barnes, 1991;
610 Murowchick, 1992; Benning et al., 2000). This pH-dependence is postulated to occur
611 as a consequence of electrostatic interactions between polysulfide species and iron
612 sulfides growth surfaces. Negative ions such as $H_2S^-$ and $S^{2-}$ are strongly attracted to
613 the sites of pyrite growth, while the protonated ends of neutral polysulfide $H_2S_2$ and
614 $H_2S^-$ favor marcasite (Tossell et al., 1981; Schoonen and Barnes 1991; Murowchick
615 1992). Polysulfide aqueous species have been suggested to form by partial oxidation
616 of aqueous $H_2S$ by chemically reactive sulfur species electron accepters (e.g.,
617 thiosulfate, Eq. 6) resulted from pre-existing pyrite oxidation reaction via Eq. 5
618 (Goldhaber et al, 1979; Murowchick and Barnes, 1986). The increasing solubility of
619 ferrous iron ($Fe^{2+}$) derived from partial oxidation of pre-existing pyrite has been
620 suggested to provide another factor favorable for marcasite precipitation (Eq. 7;

621 Granger and Warren, 1974; Goldhaber et al., 1979; Schieber and Riciputi, 2005;
622 Schieber, 2007, 2011).

623 It has been proposed that formation of marcasite would also occur either at
624 temperatures <220°C and pH<2.5 or where there is a deficiency of $S^{2-}$ under oxic or
625 anaerobic conditions (Qian et al., 2011). At Daqaio, oxidation as a factor facilitating
626 marcasite formation is favored over a deficiency of $S^{2-}$ and other S-bearing species
627 (e.g., polysulfide aqueous species) in the hydrothermal ore fluids, because numerous
628 marcasite veinlets formed, even during the late-ore stage (Fig. 2f) and the continued
629 formation of sulfides is inconsistent with a deficiency of S-bearing species. Oxidation,
630 on the other hand, is consistent with oxidation inferred from sulfur isotope evidence to
631 have been induced by fluid phase separation during multistage brecciation (Wu et al.,
632 2018a).

633

634 *5.3.3. Insights from sulfur isotopes*

635 Marcasite deposition as a consequence of oxidation is also consistent with the
636 sulfur isotopic variations observed at Daqiao deposit. A general trend of decreasing
637 $\delta^{34}S$ values obtained by both SIMS and LA-MC-ICP-MS is displayed from $Py_3$ to $Py_{4\text{-}py}$,
638 and then to $Mc_{2\text{-}py}$ and $Mc_{3\text{-}py}$ (Fig. 8). The distinct negative $\delta^{34}S$ value of $Mc_{3\text{-}py}$ is
639 also visible in the NanoSIMS profile, where the three $Mc_{3\text{-}py}$ peaks containing high Au
640 and other trace elements are coincident with the positions of $^{34}S$ depletion (Fig. 7h).

641 Fluid oxidation has been commonly suggested to play a role in gold deposition
642 and negative $\delta^{34}S$ values in sulfides (e.g., Drummond and Ohmoto, 1985; Hodkiewicz
643 et al., 2009; Tang et al., 2013; LaFlamme et al., 2018). Fractionation of heavy $^{34}S$ into

644 the oxidized sulfur species would lead to $^{34}S$ depleted $H_2S$ in the residual ore fluid,
645 and consequently pyrite and marcasite precipitated from the fluid post-oxidation
646 would be characterized by decreased $\delta^{34}S$ values relative to sulfides precipitated pre-
647 oxidation (Ohmoto, 1972). In addition, or alternatively, it has been proposed that
648 isotopically light sulfur in marcasite from hydrothermal uranium deposits (-25‰–-
649 40‰) is derived from pre-existing pyrite (>0‰), remobilized via partial oxidation to
650 soluble metastable sulfur oxyanions (Goldhaber et al., 1978; Reynolds et al., 1982).
651 It is notable that the $\delta^{34}S$ values for pyrite derived from SIMS or LA-MC-ICP-MS
652 analysis are similar (Fig. 8; mean +4.6‰ vs. +5.2‰ for $Py_3$; +2.9‰ vs. +3.4‰ for
653 $Py_{4\text{-}py}$), while those for marcasite, though showing the same trends, are different
654 (+2.4‰ vs. +5.0‰ for $Mc_{2\text{-}py}$; -1.3‰ vs. -9.7‰ for $Mc_{3\text{-}py}$). Matrix effects during
655 SIMS analysis may have contributed to this difference, given that the pyrite standard
656 was applied to correct marcasite data. The crystallographically unmatched standard
657 and analyte could cause mass bias during processes like secondary ion sputtering and
658 ionization (Riciputi et al., 1998). Further work and standard development is needed to
659 better elucidate the matrix effects during SIMS sulfur isotope analysis of marcasite.
660
661 *5.3.4. Genetic model for observed textures*
662 The textures described here are consistent with the genetic model proposed by Wu
663 et al. (2018a), where the sulfide deposition and dissolution are related to multistage
664 hydraulic fracturing. A pressure-driven genetic model for pyrite replacement at
665 Daqiao deposit is tentatively proposed (Fig. 9). In the early-ore stage deep-seated
666 fluids discharged from regional thrust faults stalled at the low-permeability Triassic

667 turbidites resulting in sulfide disseminations of $Py_3$ (Wu et al., 2018a). During
668 deposition of subhedral auriferous $Py_3$, ore fluids were probably reduced with pH >2.5
669 (Fig. 9a; cf. Granger and Warren, 1974; Murowchick and Barnes, 1986; Qian et al.,
670 2011). Temperature is thought to have been between 100°C and 240°C based on
671 microthermometry of fluid inclusions in the ore-related quartz from breccia ores (Xu
672 et al., 2015).

673 When fluid pressure exceeds the lithostatic load, accumulating shear stress creates
674 extensive hydraulic fracture permeability (Sibson et al., 1988). Fracturing could have
675 resulted in phase separation and partitioning of reduced $H_2S$ into the vapor phase to
676 produce residual fluids enriched in more oxidized sulfur species (Ohmoto, 1972;
677 Drummond and Ohmoto, 1985).

678 With the evolution of ore fluids to a more oxidizing condition, pre-existing As-
679 rich $Py_3$ started to dissolve, with reprecipitation of porous As-poor $Py_{4\text{-}py}$. Some
680 metals transferred from $Py_3$ into porous $Py_{4\text{-}py}$, others transferred into minor Cu-, Pb-,
681 and As-bearing inclusions, while others were incorporated into metal-rich solutions
682 that migrated within the system on some length scale (Fig. 9b).

683 Further oxidation of ore fluids during hydraulic fracturing led to partial dissolution
684 of the product $Py_{4\text{-}py}$ and formation of aqueous polysulfide species and then $Mc_{2\text{-}py}$
685 reprecipitation, under low pH (<2.5) and high $Fe^{2+}$ solubility conditions (Fig. 9c).
686 $Mc_{2\text{-}py}$ contains low concentrations of trace elements, plausibly because of high metal
687 solubilities in the low pH environment. Elevated concentrations of metals may have
688 been present in the interfacial solutions, since the presence of small pores and a high

proportion of fluids are thought to stabilize metals in solution at concentrations that would be considered metastable in a free fluid (Putnis et al., 1995; Putnis and Mauthe, 2001). Further brecciation and subsequent rapid fluid-pressure fluctuations may have resulted in oxidation and/or an immediate reduction in threshold supersaturation (Putnis et al., 1995). Either of these processes could trigger precipitation of the fine $Mc_{3\text{-}py}$ enriched in gold and other trace elements but depleted in $^{34}S$ (Fig. 9c).

The cyclic pressure fluctuations during this stage caused cycling precipitation between $Mc_{2\text{-}py}$ and $Mc_{3\text{-}py}$, leading to the complex-zoned $Mc_{3\text{-}py}$ within $Mc_{2\text{-}py}$ (Fig. 9c). A similar mechanism has been proposed to explain repeated high-Au negative $\delta^{34}S$ zones within individual pyrite crystals in Porgera porphyry-epithermal gold deposit, Papua New Guinea, which is thought to have formed via episodic rapid pressure release due to fault failure (Peterson and Mavrogenes, 2014).

During wall-rock readjustment after hydraulic fracturing, coarse-grained $Mc_{2\text{-}py}$ euhedra, growing from ore fluids, started to overgrow on the outside of replacement pyrite and marcasite aggregates (Fig. 9d; Sibson, 1987). After the hydrothermal deposition and sealing of the fractures, fluid pressure rebuilds and the hydraulic fracturing cycle repeats.

### 5.4. Implications for gold redistribution in fault-valve regime

Fluid cycling related to multistage hydraulic fracturing at the Daqiao gold deposit is consistent with cyclic fluid fluctuations triggered by fault-valve behavior as reported in other brittle to ductile hydrothermal systems (e.g., Sibson, 1987; Sibson et

al., 1988; Cox, 1995; Robert et al., 1995; Wilkinson and Johnston, 1996). Brittle rheological systems caused by earthquake rupturing and associated zones of brecciation have long been recognized as channels for fluid flow and as sites for high-level (1–2km) hydrothermal systems (Phillips, 1972; Sibson, 1987).

Epizonal orogenic gold mineralization (<6 km) in metamorphic belts, especially high-grade breccia ore shoots, has been proposed to record a history of incremental extensional opening and hydrothermal recementation (Hagemann et al., 1992; Gebre-Mariam et al., 1995). Mineral deposition in the extensional zones is thought to be triggered by fluid fluctuations and boiling revealed by fluid inclusion microthermometry and critical stress analyses (e.g., Phillips, 1972; Sibson, 1987; Li et al., 2002; Ostapenko and Neroda, 2007). Thermodynamic modelling reveals that removal of $H_2S$ from ore fluids into vapor phase during boiling lowers the total activity of sulfur in ore fluids, which destabilizes gold-bisulphide complexes and leads to gold deposition (Williams-Jones et al., 2009).

However, few previous studies have focused on the sequence of hydrothermal events, sulfide replacement and related metal redistribution in episodically evolving hydrothermal systems. Exceptions include a LA-ICP-MS in-situ sulfur isotope study of ore-related pyrite in dilational structures from orogenic gold deposits, Yilgarn Craton, where negative $\delta^{34}S$ values were suggested to be a result of fluid-pressure fluctuations associated with fault-valve cycling (Hodkiewicz et al., 2009). In a later study, Rottier et al. (2016) proposed that a progressive increase of $f_{S2}$, $f_{O2}$, and pH in ore fluids from epithermal systems in Peru, drove replacement of pyrrhotite and

arsenopyrite by marcasite and pyrite via a dissolution-reprecipitation mechanism associated with systematic redistribution of trace elements. At the Daqiao deposit, a combination of LA-ICP-MS, SIMS and NanoSIMS analyses record the micron- to nano-scale, complex-zoned redistribution and re-enrichment of gold plus other trace metals during a two-step replacement process related to multistage hydraulic fracturing.

The results emphasize the key role of brittle rheological regimes caused by the fault-valve activity not only in gold deposition, but also in redistribution and re-enrichment of gold and other metals in high-level hydrothermal gold systems worldwide. If, as we suggest, ore fluids in these hydrothermal systems began to partially oxidize during abrupt pressure decreases and fluctuations associated with hydraulic brecciation, pre-existing auriferous pyrite could dissolve and form zoned gold-rich marcasite. Complex zoning in marcasite indicate that this replacement is controlled by episodic processes, plausibly, such as infiltration of hydrothermal fluids in response to pressure variation.

## 6. CONCLUSIONS

Detailed microscopic observations as well as the geochemical data presented in this study indicate that the replacement of auriferous pyrite at the Daqiao epizonal orogenic deposit mainly proceeded via a two-step dissolution and reprecipitation replacement process plus additional marcasite overgrowth.

Results of LA-ICP-MS and NanoSIMS analyses suggest that gold and other trace

elements (Te, Se, Zn, Co, Tl, Ni, W, and As) originally incorporated in parent $Py_3$ are partly expelled and remobilized during replacement by porous $Py_{4\text{-}py}$. Other metals (Cu, Sb, Ag, Pb, and Bi) mainly occurring as mineral inclusions, show enrichment in $Py_{4\text{-}py}$. In the replacement of $Py_{4\text{-}py}$ by aggregates of $Mc_{2\text{-}py}$, $Mc_{3\text{-}py}$ and minor arsenopyrite, $Mc_{2\text{-}py}$ is deficient in metals, while metals (W, Tl, Au, As, Sb, Ag, Se, and Zn) are enriched in zoned $Mc_{3\text{-}py}$.

The textures observed at Daqiao deposit provide a record of evolving $f_{O2}$ and pH in ore fluids. Four steps are proposed for the process of replacement and precipitation of various sulfides and sulfarsenides: (1) $Py_3$ precipitation; (2) partial dissolution of $Py_3$ and reprecipitation of $Py_{4\text{-}py}$ with metal redistribution under increasing $f_{O2}$; (3) partial dissolution of $Py_{4\text{-}py}$ with reprecipitation of metal-poor $Mc_{2\text{-}py}$ and cyclic reprecipitation of metal-rich zoned $Mc_{3\text{-}py}$ plus minor arsenopyrite via a reduction in threshold supersaturation; and (4) overgrowth of $Mc_{2\text{-}py}$.

Similar to findings elsewhere, episodically pressure-driven hydrothermal movement in brittle rheological zones triggered by fault-valve behavior is thought to be critical in the formation of the Daqiao epizonal orogenic gold deposit. This study further quantitatively emphasizes the pressure-driven process plays a key role in the micron- to nano-scale, complex-zoned redistribution and re-enrichment of gold and other metals during the replacement of auriferous pyrite.

## ACKNOWLEDGEMENTS

The authors acknowledge Xiao-Ye Jin and Lei Chen for their help during LA-ICP-

MS trace element and SIMS sulfur isotope analysis, respectively. The Daqiao Mining Ltd. and Geological Survey of Gansu Province are also thanked for excellent field assistance. Research work was financially supported by the National Natural Science Foundation of China (grants 41772081, 41325007 and 41072057), the Fundamental Research Funds for the Central Universities, China University of Geosciences, Wuhan (CUGCJ1711), and the GPMR State Key Laboratory (MSFGPMR03). The senior author acknowledges the receipt of Chinese Scholarship Council/Curtin International Postgraduate Research Scholarship. This is contribution 10 from CUG Center for Research in Economic Geology and Exploration Targeting (CREGET). This paper greatly benefited from constructive and thorough reviews from Crystal LaFlamme and an anonymous reviewer. Ours thanks go to editorial suggestions from Marc Norman and Edward M. Ripley.

## REFERENCES

Altree-Williams A., Pring A., Ngothai Y. and Brugger J. (2015) Textural and compositional complexities resulting from coupled dissolution-reprecipitation reactions in geomaterials. *Earth Sci. Rev.* **150**, 628-651.

Arehart G. B., Eldridge C. S., Chryssoulis S. L. and Kesler S. E. (1993) Ion microprobe determination of sulfur isotope variations in iron sulfides from the Post/Betze sediment-hosted disseminated gold deposit, Nevada, USA. *Geochim. Cosmochim. Acta* **57**, 1505-1519.

Benning L. G., Wilkin R. T. and Barnes H. L. (2000) Reaction pathways in the Fe-S system below 100 °C. *Chem. Geol.* **167**, 25-51.

Blanchard M., Alfredsson M., Brodholt J., Wright K. and Catlow C. R. A. (2007). Arsenic incorporation into $FeS_2$ pyrite and its influence on dissolution: a DFT study. *Geochim. Cosmochim. Acta* **71**, 624-630.

Brugger J., McFadden A., Lenehan C. E., Etschmann B., Xia F., Zhao J. and Pring A. (2010) A novel route for the synthesis of mesoporous and low-thermal stability materials by coupled dissolution-reprecipitation reactions: mimicking hydrothermal mineral formation. *Chimia* **64**, 693-698.

Butler I. B. and Rickard D. (2000) Framboidal pyrite formation via the oxidation of iron (II)

monosulfide by hydrogen sulfide. *Geochim. Cosmochim. Acta* **64**, 2665-2672.

Chen L., Li X. H., Li J. W., Hofstra A. H., Liu Y. and Koenig A. E. (2015) Extreme variation of sulfur isotopic compositions in pyrite from the Qiuling sediment-hosted gold deposit, West Qinling orogen, central China: an in situ SIMS study with implications for the source of sulfur. *Miner. Deposita* **50**, 643-656.

Chen W. T., Zhou M. F., Li X., Gao J. F., Bao Z. and Yuan H. (2018). In situ Pb-Pb isotopic dating of sulfides from hydrothermal deposits: a case study of the Lala Fe-Cu deposit, SW China. *Miner.* **53**, *Deposita* https://doi.org/10.1007/s00126-018-0833-1

Cline J. S. (2001) Timing of gold and arsenic sulfide mineral deposition at the Getchell Carlin-type gold deposit, north-central Nevada. *Econ. Geol.* **96**, 75-89.

Cook N. J., Ciobanu C. L. and Mao J. W. (2009) Textural control on gold distribution in As-free pyrite from the Dongping, Huangtuliang and Hougou gold deposits, North China Craton (Hebei Province, China). *Chem. Geol.* **264**, 101-121.

Cook N. J., Ciobanu C. L., Meria D., Silcock D. and Wade B. (2013) Arsenopyrite-pyrite association in an orogenic gold ore: Tracing mineralization history from textures and trace elements. *Econ. Geol.* **108**, 1273-1283.

Cox S. F. (1995). Faulting processes at high fluid pressures: an example of fault valve behavior from the Wattle Gully Fault, Victoria, Australia. *J. Geophys. Res*. **100**, 12841-12859.

Deditius A. P., Utsunomiya S., Renock D., Ewing R. C., Ramana C. V., Becher U. and Kesler S. E. (2008) A proposed new type of arsenian pyrite: Composition, nanostructure and geological significance. *Geochim. Cosmochim. Acta* **72**, 2919-2933.

Dong Y. P, Zhang G. W., Neubauer F., Liu X., Genser J. and Hauzenberger C. (2011) Tectonic evolution of the Qinling orogen, China: Review and synthesis. *J. Asian Earth Sci.* **41**, 213-237.

Dong Y., Yang Z., Liu X., Sun S., Li W., Cheng, B., Zhang F., Zhang X., He D. and Zhang, G. (2016). Mesozoic intracontinental orogeny in the Qinling Mountains, central China. *Gondwana Res*. **30**, 144-158.

Drummond S. E. and Ohmoto H. (1985) Chemical evolution and mineral deposition in boiling hydrothermal systems. *Econ. Geol.* **80**, 126-147.

Dubé B., Williamson K., McNicoll V., Malo M., Skulski T., Twomey T. and Sanborn-Barrie M. (2004) Timing of gold mineralization at Red Lake, Northwestern Ontario, Canada: New constraints from U-Pb geochronology at the Goldcorp high-grade zone, Red Lake mine, and the Madsen mine. *Econ. Geol*. **99**, 1611-1641.

Evans K. A., Tomkin A. G., Cliff J. and Fiorentini M. L. (2014). Insights into subduction zone sulfur recycling from isotopic analysis of eclogite-hosted sulfides. *Chem. Geol.* **365**, 1-19.

Farquhar J., Cliff J., Zerkle A. L., Kamyshny A., Poulton S. W., Claire M., Adams D. and Harms B. (2013) Pathways for Neoarchean pyrite formation constrained by mass-independent sulfur isotopes. Proc. *Natl. Acad. Sci. USA* **110**, 17638-17643.

Fleet M. E. (1970) Structural aspects of the marcasite-pyrite transformation. *Can. Mineral.* **10**, 225-231.Fleet M. E. and Mumin A. H. (1997) Gold-bearing arsenian pyrite and marcasite and arsenopyrite from Carlin Trend gold deposits and laboratory synthesis. *Am. Mineral.* **82**, 182-193.

Fougerouse D., Micklethwaite, S., Tomkins A. G., Mei Y., Kilburn M., Guagliardo P., Fisher L. A., Halfpenny A., Gee M., Paterson D. and Howard D. L. (2016) Gold remobilisation and formation of high grade ore shoots driven by dissolution-reprecipitation replacement and Ni substitution into auriferous arsenopyrite. *Geochim. Cosmochim. Acta* **178**, 143-159.

Fougerouse D., Micklethwaite S., Ulrich S., Miller J., Godel B., Adams D. T. and McCuaig T. C. (2017) Evidence for two stages of mineralization in West Africa's largest gold deposit: Obuasi, Ghana. *Econ. Geol.* **112**, 3-22

Franchini M., Mcfarlane C., Maydagán L., Reich M., Lentz D., Meinert L. and Bouhier V. (2015) Trace metals in pyrite and marcasite from the Agua Rica porphyry-high sulfidation epithermal deposit, Catamarca, Argentina: Textural features and metal zoning at the porphyry to epithermal transition. *Ore Geol. Rev.* **66**, 366-387.

Gao S., Huang F., Gu X., Chen Z., Xing M. and Li Y. (2017). Research on the growth orientation of pyrite grains in the colloform textures in Baiyunpu Pb–Zn polymetallic deposit, Hunan, China. *Miner. Petrol.* **111**, 69-79.

Gebre-Mariam M., Hagemann S. G. and Groves D. I. (1995) A classification scheme for epigenetic Archaean lode-gold deposits. *Miner. Deposita* **30**, 408-410.

Geisler T., Schaltegger U. and Tomaschek F. (2007) Re-equilibration of zircon in aqueous fluids and melts. *Elements* **3**, 43-50.

Goldhaber M. B., Reynolds R. L. and Rye R. O. (1978) Origin of a South Texas roll-type deposit; II, Sulfide petrology and sulfur isotope studies. *Econ. Geol*. **73**, 1690-1705.

Goldhaber M. B. Reynolds R. L. and Rye R. O. (1979) Formation and resulfidization of a South Texas roll-type uranium deposit. *USGS Open File Report*. 79-1651.

Granger H. C. and Warren C. G. (1974) Zoning in the altered tongue associated with roll-type uranium deposits, in Formation of uranium ore deposits. In *Formation of Uranium Ore Deposits* (Chairman R. D. Nininger), *I.A.E.A., Proc. Ser*., No. STI/PUB/374, pp. 185-200.

Hagemann S. G., Groves D. I., Ridley J. R. and Vearncombe J. R. (1992) The Archean lode gold deposits at Wiluna, Western Australia; high-level brittle-style mineralization in a strike-slip regime. *Econ. Geol.* **87**, 1022-1053.

Harlov D. E., Wirth R. and Hetherington C. J. (2011) Fluid-mediated partial alteration in monazite: the role of coupled dissolution-reprecipitation in element redistribution and mass transfer. *Contrib. Mineral. Petrol.* **162**, 329-348.

Higgins N. C. (1980) Fluid inclusion evidence for the transport of tungsten by carbonate complexes in hydrothermal solutions. *Can. J. Earth Sci.***17**, 823-830.

Hodkiewicz P. F., Groves D. I., Davidson G. J., Weinberg R.F. and Hagemann S.G. (2009) Influence of structural setting on sulphur isotopes in Archean orogenic gold deposits, Eastern Goldfields Province, Yilgarn, Western Australia. *Miner Deposita.* **44**, 129-150.

LaFlamme C., Martin L., Jeon H., Reddy S., Selvaraja V., Caruso S., Hao T. B., Roberts M. P., Voute F., Hagemann S., Wacey D., Littman S., Wing B., Fiorentini M. and Kilburn M. R. (2016) In situ multiple sulfur isotope analysis by SIMS of pyrrhotite, pentlandite and chalcopyrite to refine magmatic ore genetic models. *Chem. Geol*. **444**, 1-15.

LaFlamme C., Sugiono D., Thébaud N., Caruso S., Fiorentini M., Selvaraja V., Jeon H., Voute F. Martin L. (2018) Multiple sulfur isotopes monitor fluid evolution in an orogenic gold deposit. *Geochim Cosmochim Acta* **222**:436-446.

Large R. R., Maslennikon V. V., Robert F., Danyushevsky L. V. and Chang Z.S. (2007) Multistage sedimentary and metamorphic origin of pyrite and gold in the giant Sukhoi Log deposit, Lena gold province, Russia. *Econ. Geol.* **102**, 1233-1267.

Large R. R., Danyushevsky L., Hollit C., Maslennikov V., Meffre S., Gilbert S., Bull S., Scott R., Embsbo P., Thomas H., Singh B. and Foster J. (2009) Gold and trace element zonation in pyrite

using a laser imaging technique: Implications for the timing of gold in orogenic and Carlin style sediment-hosted deposits. *Econ. Geol.* **104**, 635-668.

Lennie A. R. and Vaughan D. J. (1992) Kinetics of the marcasite-pyrite transformation: An infrared spectroscopic study. *Am. Mineral.* **77**, 1166-1171.

Li J. W., Zhou M. F., Li X. F., Li Z. J. and Fu Z. R. (2002) Origin of a large breccia-vein system in the Sanerlin uranium deposit, southern China: a reinterpretation. *Miner. Deposita* **37**, 213-225.

Lippmann F. (1980) Phase diagrams depicting aqueous solubility of binary mineral systems. *Neues Jahrb. Mineral. Abh*. **139**, 1–25.

Liu S. G., Li Z. W., Liu S., Luo Y. H., Xu G. Q., Dai G. H., Gong C. M. and Yong Z.Q. (2006). Formation and evolution of Dabashan foreland basin and fold-and-thrust belt. Geological Publishing House, Sichuan, China, pp. 1–248.

Li X. H., Fan H. R., Yang K. F., Hollings P., Liu, X., Hu, F. F. and Cai, Y. C. (2018). Pyrite textures and compositions from the Zhuangzi Au deposit, southeastern North China Craton: implication for ore-forming processes. *Contrib. Mineral. Petrol*. **173**, 73. https://doi.org/10.1007/s00410-018-1501-2

Mao J. W., Qiu Y. M., Goldfarb R. J., Zhang Z. C, Garwin S. and Fengshou R. (2002) Geology, distribution, and classification of gold deposits in the western Qinling belt, central China. *Miner. Deposita* **37**, 352-377.

Meng Q. R. and Zhang G. W. (1999) Timing of collision of the North and South China blocks: Controversy and reconciliation. *Geology* **27**, 123-126.

McLoughlin N., Wacey D., Kruber C., Kilburn M. R., Thorseth I. H. and Pedersen R. B. (2011) A combined TEM and NanoSIMS study of endolithic microfossils in altered seafloor basalt. *Chem. Geol.* **289**, 154-162.

Morey A. A., Tomkins A. G., Bierlein F. P., Weinberg R. F. and Davidson G. J. (2008) Bimodal Distribution of Gold in Pyrite and Arsenopyrite: Examples from the Archean Boorara and Bardoc Shear Systems, Yilgarn Craton, Western Australia. *Econ. Geol.* **103**, 599-614.

Murowchick J. B. and Barnes H. L. (1986) Marcasite precipitation from hydrothermal solutions. *Geochim. Cosmochim. Acta* **50**, 2615-2629.

Murowchick J. B. (1992) Marcasite inversion and the petrographic determination of pyrite ancestry. *Econ. Geol.* **87**, 1141-1152.

Ohmoto H. (1972) Systematics of sulfur and carbon isotopes in hydrothermal ore deposits *Econ. Geol.* **67**, 551-578.

Ostapenko N. S. and Neroda O. N. (2007) Fluid pressure and hydraulic fracturing in hydrothermal ore formation at gold deposits. *Russ. J. Pac. Geol.* **1**, 276-289.

Pal D. C., Sarkar S., Mishra B. and Sarangi A. K. (2011). Chemical and sulphur isotope compositions of pyrite in the Jaduguda U (-Cu-Fe) deposit, Singhbhum shear zone, eastern India: Implications for sulphide mineralization. *J. Earth Syst. Sci.* **120**, 475-488.

Pals D. W., Spry P. G. and Chryssoulis S. (2003) Invisible gold and tellurium in arsenic-rich pyrite from the Emperor gold deposit, Fiji: implications for gold distribution and deposition. *Econ. Geol.* **98**, 479-493.

Peterson E. C. and Mavrogenes J. A. (2014) Linking high-grade gold mineralisation to earthquake-induced fault-valve processes in the Porgera gold deposit, Papua New Guinea. *Geology* **42**, 383-386.

Phillips W. J. (1972) Hydraulic fracturing and mineralization. *J. Geol. Soc. London*. **128**, 337-59.Putnis A., Prieto M. and Fernandez-Diaz L. (1995) Fluid supersaturation and crystallization in porous

939 media. *Mineral. Mag.* **132**, 1-13.
940 Putnis A. and Mauthe G. (2001) The effect of pore size on cementation in porous rocks. *Geofluids* **1**,
941 37-41.
942 Putnis A. (2002) Mineral replacement reactions: from macroscopic observations to microscopic
943 mechanisms. *Mineral. Mag.* **66**, 689-708.
944 Putnis A. (2009) Mineral replacement reactions. *Rev. Mineral. Geochem.* **70**, 87-124.
945 Qian G., Brugger J., SkinnerW. M., Chen G. and Pring A. (2010) An experimental study of the
946 mechanism of the replacement of magnetite by pyrite up to 300 °C. *Geochim. Cosmochim. Acta* **74**,
947 5610-5630.
948 Qian G., Xia F., Brugger J., Skinner W., Bei J., Chen G. and Pring A. (2011) Replacement of pyrrhotite
949 by pyrite and marcasite under hydrothermal conditions up to 220 °C: An experimental study of
950 reaction textures and mechanisms. *Am. Mineral.* **96**, 1878-1893.
951 Reed M.H. and Palandri J. (2006) Sulfide mineral precipitation from hydrothermal fluids. *Rev. Mineral.*
952 *Geochem.* **61**, 609-631.
953 Reich M., Kesler S. E., Utsunomiya S., Palenik C. S., Chryssoulis S. L. and Ewing R. C. (2005)
954 Solubility of gold in arsenian pyrite. *Geochim. Cosmochim. Acta* **69**, 2781–2796.
955 Reynolds R. L., Goldhaber M. B. and Carpenter D. J. (1982) Biogenic and nonbiogenic ore-forming
956 processes in the South Texas uranium district: Evidence from the Panna Maria deposit. *Econ. Geol.*
957 **77**, 541-556.
958 Riciputi L. R., Paterson B. A. and Ripperdan R. L. (1998) Measurements of light stable isotope ratios
959 by SIMS: Matrix effects for oxygen, carbon, and sulfur isotopes in minerals. *Int. J. Mass Spec*. **178**,
960 81–112
961 Robert F., Boullier A. M. and Firdaous K. (1995). Gold-quartz veins in metamorphic terranes and their
962 bearing on the role of fluids in faulting. *J. Geophys. Res*. **100**, 12861-12879.
963 Rottier B., Kouzmanov K., Wälle M., Bendezú R. and Fontboté L. (2016) Sulfide Replacement
964 Processes Revealed by Textural and LA-ICP-MS Trace Element Analyses: Example from the Early
965 Mineralization Stages at Cerro de Pasco, Peru. *Econ. Geol*. **111**, 1347-1367.
966 Rouxel O., Ono S. H., Alt J., Rumble D. and Ludden J. (2008) Sulfur isotope evidence for microbial
967 sulfate reduction in altered oceanic basalts at ODP Site 801. *Earth Planet Sci. Lett*. **268**, 110–123.
968 Rubatto D., Müntener O., Barnhoorn A. and Gregory C. (2008) Dissolution-reprecipitation of zircon at
969 low-temperature, high-pressure conditions (Lanzo Massif, Italy). *Am. Mineral*. **93**, 1519-1529.
970 Schieber J. and Riciputi L. (2005) Pyrite and Marcasite Coated Grains in the Ordovician Winnipeg
971 Formation, Canada: An Intertwined Record of Surface Conditions, Stratigraphic Condensation,
972 Geochemical “Reworking”, and Microbial Activity. *J. Sediment. Res.* **75**, 907-920.
973 Schieber J. (2007) Oxidation of detrital pyrite as a cause for Marcasite Formation in marine lag
974 deposits from the Devonian of the eastern US. *Deep-Sea Res. II Top. Stud. Oceanogr.* **54**, 1312-
975 1326.
976 Schieber J. (2011) Marcasite in Black Shales—a Mineral Proxy for Oxygenated Bottom Waters and
977 Intermittent Oxidation of Carbonaceous Muds. *J. Sediment. Res.* **81**, 447-458.
978 Schoonen M. A. A. and Barnes H. L. (1991) Reactions forming pyrite and marcasite from solution: II.
979 Via FeS precursor below 100 °C. *Geochim. Cosmochim. Acta* **55**, 1505-1514.
980 Selvaraja V., Fiorentini M. L., Jeon H., Savard D. D., LaFlamme C. K., Guagliardo P., Caruso S. and
981 Bui T. H. (2017). Evidence of local sourcing of sulfur and gold in an Archaean sediment-hosted
982 gold deposit. *Ore Geol. Rev.* **89**, 909-930.

Smith K. S. (1999) Metal sorption on mineral surfaces: an overview with examples relating to mineral deposits. *Rev. Econ. Geol.* **6**, 161-82.

Sibson R. H. (1987) Earthquake rupturing as a mineralizing agent in hydrothermal systems. *Geology* 15, 701-704.

Sibson R. H. Robert F. and Poulsen K. H. (1988). High-angle reverse faults, fluid-pressure cycling, and mesothermal gold-quartz deposits. *Geology* **16**, 551-555.

Simon G., Kesler S. E. and Chryssoulis S. (1999). Geochemistry and textures of gold-bearing arsenian pyrite, Twin Creeks, Nevada; implications for deposition of gold in Carlin-type deposits. *Econ. Geol*. **94**, 405-421.

Stumm W. and Morgan J. J. (1996) *Aquatic chemistry*, third ed. Wiley-Interscience, New York.Su W., Xia B., Zhang H., Zhang X. and Hu R. (2008). Visible gold in arsenian pyrite at the Shuiyindong Carlin-type gold deposit, Guizhou, China: Implications for the environment and processes of ore formation. *Ore Geol. Rev*. **33**, 667-679.

Sung Y. H., Brugger J., Ciobanu C. L., Pring A., Skinner W. and Nugus M. (2009) Invisible gold in arsenian pyrite and arsenopyrite from a multistage Archaean gold deposit: Sunrise Dam, Eastern Goldfields Province, Western Australia. *Miner. Deposita* **44**, 765-791.

Tang K. F., Li J. W., Selby D., Zhou M. F., Bi S.J. and Deng X. D. (2013) Geology, mineralization, and geochronology of the Qianhe gold deposit, Xiong'ershan area, southern North China Craton. *Miner. Deposita* **48**, 729-747.

Thomas H. V., Large R. R., Bull S. W., Maslennikov V., Berry R. F., Fraser R., Froud S. and Moye R. (2011) Pyrite and Pyrrhotite Textures and Composition in Sediments, Laminated Quartz Veins, and Reefs at Bendigo Gold Mine, Australia: Insights for Ore Genesis. *Econ. Geol.* **106**, 1-31.

Tomkins A. G. and Mavrogenes J. A. (2001) Redistribution of Gold within Arsenopyrite and Löllingite during Pro- and Retrograde Metamorphism: Application to Timing of Mineralization. *Econ. Geol.* **96**, 525-534.

Tomkins A. G., Pattison D. R. M. and Frost B. R. (2007) On the Initiation of Metamorphic Sulfide Anatexis. *J. Petrol.* **48**, 511-535.

Tossell J. A., Vaughan D. J. and Burdett J. K. (1981) Pyrite, marcasite, and arsenopyrite type minerals: crystal chemical and structural principles. *Phys. Chem. Minerals* **7**, 177-184.

Walker F. D. L., Lee M. R. and Parsons I. (1995) Micropores and micropermeable texture in alkali feldspars: geochemical and geophysical implications. *Mineral. Mag.* **59**, 505-534.

Wen G., Li J. W., Hofstra A. H., Koenig A. E., Lowers H. A. and Adams, D. (2017). Hydrothermal reequilibration of igneous magnetite in altered granitic plutons and its implications for magnetite classification schemes: Insights from the Handan-Xingtai iron district, North China Craton. *Geochim. Cosmochim. Acta* **213**, 255-270.

Whitehouse M. J. (2013) Multiple sulfur isotope determination by SIMS: evaluation of reference sulfides for $\Delta^{33}S$ with observations and a case study on the determination of $\Delta^{36}S$. *Geostand Geoanal. Res.* **37**, 19-33

Widler A. M. and Seward T. M. (2002) The adsorption of gold (I) hydrosulphide complexes by iron sulphide surfaces. *Geochim. Cosmochim. Acta* **66**, 383-402.

Wilkinson J. J. and Johnston J. D. (1996). Pressure fluctuations, phase separation, and gold precipitation during seismic fracture propagation. *Geology* **24**, 395-398.

Williams-Jones A. E., Bowell R. J. and Migdisov A. A. (2009) Gold in solution. *Elements*. **5**: 281-287.

Wong K. H., Zhou M. F., Chen W. T., O'Brien H., Lahaye Y. and Chan S. L. J. (2017) Constraints of

fluid inclusions and in-situ S-Pb isotopic compositions on the origin of the North Kostobe sediment-hosted gold deposit, eastern Kazakhstan. *Ore Geol. Rev.* **81**, 256-269.

Wu Y. F., Li J. W., Evans, K., Koeing A. E., Li Z. K., O'Brien H., Lahaye Y., Rempel K., Hu S. Y., Zhang Z. P. and Yu J. P. (2018a) Ore-Forming Processes of the Daqiao Epizonal Orogenic Gold Deposit, West Qinling Orogen, China: Constraints from Textures, Trace Elements and Sulfur Isotopes of Pyrite and Marcasite, and Raman Spectroscopy of Carbonaceous Material. *Econ. Geol.* **113**, 1093-1132.

Wu Y. F., Li J. W., Evans K., Vasconcelos P. M., Thiede, D. S., Fougerouse D. and Rempel K. (2018b). Late Jurassic to Early Cretaceous age of the Daqiao gold deposit, West Qinling Orogen, China: Implications for regional metallogeny. *Miner. Deposita* **53**. https://doi.org/10.1007/s00126-018-0835-z

Xia F., Brugger J., Chen G., Ngothai Y., O'Neill B., Putnis A. and Pring A. (2009) Mechanism and kinetics of pseudomorphic mineral replacement reactions: A case study of the replacement of pentlandite by violarite. *Geochim. Cosmochim. Acta*, **73**, 1945-1969.

Xu L., Wu B. X., Wang Y. L., Wang Z. X., Wang G. and Sun Z.P. (2015) Fluid inclusion characteristics and geological significance at Daqiao gold deposit. *J. Jilin Univ*. **45**, 568-569.

Yan J., Hu R., Liu S., Lin Y., Zhang J. and Fu S. (2018) NanoSIMS element mapping and sulfur isotope analysis of Au-bearing pyrite from Lannigou Carlin-type Au deposit in SW China: New insights into the origin and evolution of Au-bearing fluids. *Ore Geol. Rev.* **92**, 29–41.

Yang H. X. and Downs R. T. (2008) Crystal structure of glaucodot, (Co, Fe) AsS, and its relationships to marcasite and arsenopyrite. *Am. Mineral.* **93**, 1183-1186.

Zeng Q. T., McCuaig T. C., Tohver E., Bagas L. and Lu Y. J. (2014). Episodic Triassic magmatism in the western South Qinling Orogen, central China, and its implications. *Geol. J*. **49**, 402-423.

Zhao J., Brugger J., Chen G., Ngothai Y. and Pring, A. (2014). Experimental study of the formation of chalcopyrite and bornite via the sulfidation of hematite: mineral replacements with a large volume increase. *Am. Mineral.* **99**, 343-354.

## Figure and table captions

**Fig. 1.** (a) A simplified map showing tectonic division of the Qinling Orogen. Also shown are the major faults, gold deposits and the location of Daqiao (modified from Wu et al., 2018a). The insert indicates the location of the West Qinling Orogen in China. (b) Geology of the Daqiao gold deposit.

**Fig. 2.** Photographs illustrating textures of breccia ores of the Daqiao gold deposit. (a) Typical auriferous silicified tectonic breccia A. (b) Fine-grained pyrite (Py) and marcasite (Mc) disseminations in silicified tectonic breccias A. (c) Hydraulic limestone breccias cemented by coarse calcite (Cc) veins. (d) Multistage hydraulic brecciation first cemented by quartz (Qz) and then by calcite. (e) Black silicified breccia A cemented by quartz and sulfides forming breccia B and then filled with

calcite-chalcedony (Cal)-marcasite matrix (breccia C). (f) Late-ore stage marcasite-calcite veinlets in altered slate.

**Fig. 3.** Typical textures and overprinting relationships of different generations of pyrite and marcasite at Daqiao deposit. (a-d) Inclusion-free, zoned pyrite ($Py_3$) is surrounded by porous pyrite ($Py_{4\text{-}py}$) plus minor chalcopyrite (Ccp), galena (Gn), and arsenopyrite (Apy) inclusions. Note the sharp and curvilinear interfaces among them (contacts marked with yellow lines). (e and f) $Py_{4\text{-}py}$ borders $Py_3$ and is also present in $Py_3$ microfractures and interstitial spaces between $Py_3$ grains; $Py_{4\text{-}py}$ is in turn bordered by aggregates of marcasite ($Mc_{2\text{-}py}$ and $Mc_{3\text{-}py}$; contact marked by red lines). (g and h) Marcasite ($Mc_{2\text{-}py}$ and $Mc_{3\text{-}py}$) containing irregular $Py_{4\text{-}py}$ inclusions shows similar external morphology with euhedral $Py_{4\text{-}py}$ grains. (i) Marcasite ($Mc_{2\text{-}py}$ and $Mc_{3\text{-}py}$) and arsenopyrite (Apy) veinlets and inclusions in porous $Py_{4\text{-}py}$ that presents in the microfractures and margins of $Py_3$. (j) Close-up of intergrowth of marcasite and Apy inclusions. (k) $Mc_{2\text{-}py}$ and $Mc_{3\text{-}py}$ are characterized by a bimodal grain size distribution with a fine and a coarse grained domain (contact marked by white lines) bordering porous $Py_{4\text{-}py}$. (l) Bright zoned $Mc_{3\text{-}py}$, Apy and $Mc_{2\text{-}py}$ euhedras occurs as aggregates surrounding $Py_{4\text{-}py}$ in the fine-grained domain. (m) Bright, sub-micron sector and cyclic bands of $Mc_{3\text{-}py}$ in $Mc_{2\text{-}py}$. Scale bar is 30 μm.

**Fig. 4.** Diagrams showing results of LA-ICP-MS spot analysis on the different generations of pyrite and marcasite. (a) Au-As. (b) Au-Ag. (c) Cu-Zn. (d) Sb-Tl. (e) Co-Ni. (f) Pb-Bi.

**Fig. 5.** (a and b) Comparisons of typical sulfide textures involving co-existing $Py_3$, $Py_{4\text{-}py}$ and marcasite ($Mc_{2\text{-}py}$ and $Mc_{3\text{-}py}$) under reflected microscopy and SEM. (c and d) LA-ICP-MS profiles showing the trace element variations across different sulfides as shown on (a) and (c), respectively.

**Fig. 6.** Spider diagrams illustrating the gain and loss of trace elements during the $Py_3$ (a) and $Py_{4\text{-}py}$ (b) replacement processes.

**Fig. 7.** NanoSIMS ion maps (b-g) from the boxed area of sulfide aggregate (a) of

sulfur (**(**$^{34}$S), copper ($^{63}$Cu$^{32}$S), nickel ($^{60}$Ni$^{32}$S), arsenic ($^{75}$As$^{32}$S), antimony ($^{123}$Sb), and gold ($^{197}$Au) showing the trace element distribution during pyrite replacement, and line profile (h) showing the trace element variation patterns.

**Fig. 8.** Box figure (a) and histogram (b) showing the variation of $\delta^{34}$S values of different generations of pyrite and marcasite involved in the pyrite replacement.

**Fig. 9.** Schematic diagram of the pressure-driven two-step replacement process of pyrite, subsequent marcasite overgrowth and associated remobilization of gold and other trace metals at the Daqiao gold deposit. See text for explanations.

**Table 1.** Comparison between diagnostic features of dissolution and reprecipitation, overgrowth, solid-state diffusion, and sulfide textures from the Daqiao gold deposit

**Table 2.** Summarized LA-ICP-MS analyses of different generations of pyrite and marcasite involved in the pyrite replacement from the Daqiao gold deposit

## APPENDIX A

Standard and specific details of each methodology.

## APPENDIX B

**Table B.1.** LA-ICP-MS analyses of different generations of pyrite and marcasite involved in the pyrite replacement from the Daqiao gold deposit

**Table B.2.** SIMS in-situ sulfur isotope compositions of different generations of pyrite and marcasite involved in the pyrite replacement from the Daqiao gold deposit

**Fig. 1**

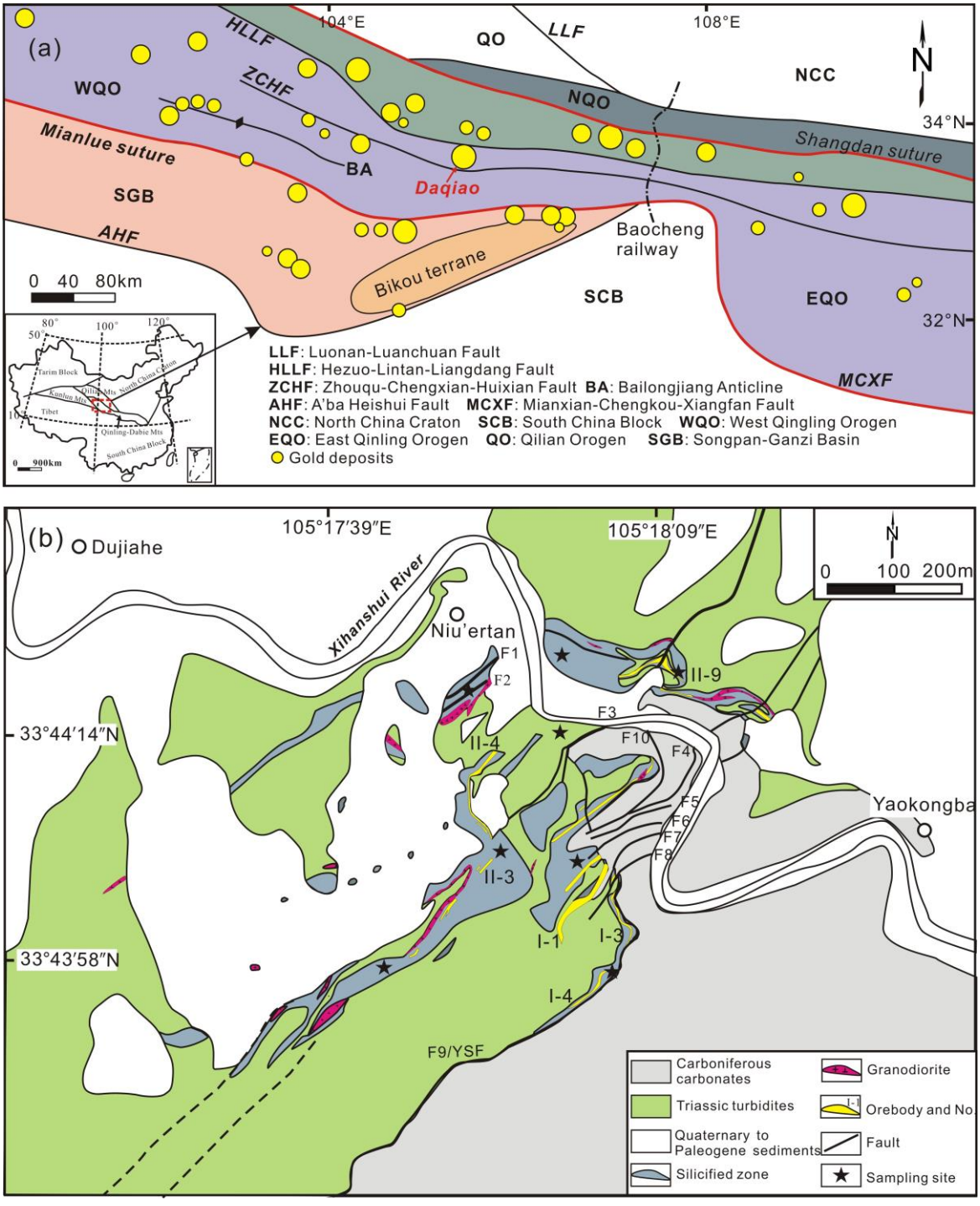
(a)
104°E
108°E
QO
LLF
NCC
HLLF
ZCHF
WQO
NQO
34°N
Shangdan suture
Mianlue suture
BA
Daqiao
SGB
AHF
Baocheng railway
Bikou terrane
SCB
EQO
32°N
MCXF
0 40 80km
LLF: Luonan-Luanchuan Fault
HLLF: Hezuo-Lintan-Liangdang Fault
ZCHF: Zhouqu-Chengxian-Huixian Fault BA: Bailongjiang Anticline
AHF: A'ba Heishui Fault MCXF: Mianxian-Chengkou-Xiangfan Fault
NCC: North China Craton SCB: South China Block WQO: West Qinling Orogen
EQO: East Qinling Orogen QO: Qilian Orogen SGB: Songpan-Ganzi Basin
Gold deposits
(b) Dujiahe
105°17′39″E
105°18′09″E
0 100 200m
Xihanshui River
Niu'ertan
F1
F2
F3
F10
F4
II-9
II-4
33°44′14″N
F5
F6
F7
F8
Yaokongba
II-3
I-1
I-3
33°43′58″N
I-4
F9/YSF
Carboniferous carbonates
Triassic turbidites
Quaternary to Paleogene sediments
Silicified zone
Granodiorite
Orebody and No.
Fault
Sampling site

**Fig. 2**

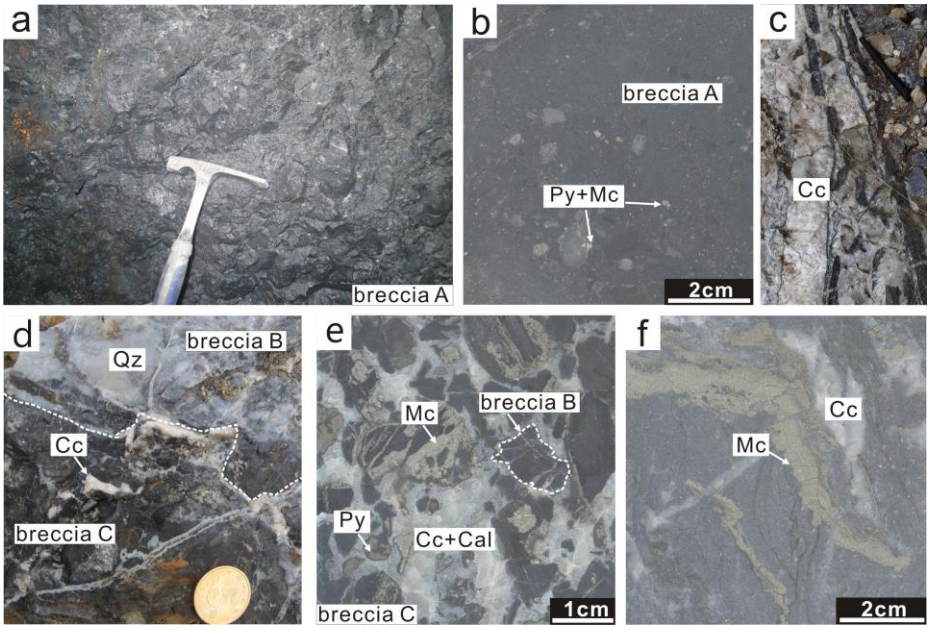
a
breccia A
b
breccia A
Py+Mc
2cm
c
Cc
d
Qz
breccia B
Cc
breccia C
e
Mc
breccia B
Py
Cc+Cal
breccia C
1cm
f
Cc
Mc
2cm

**Fig. 3**

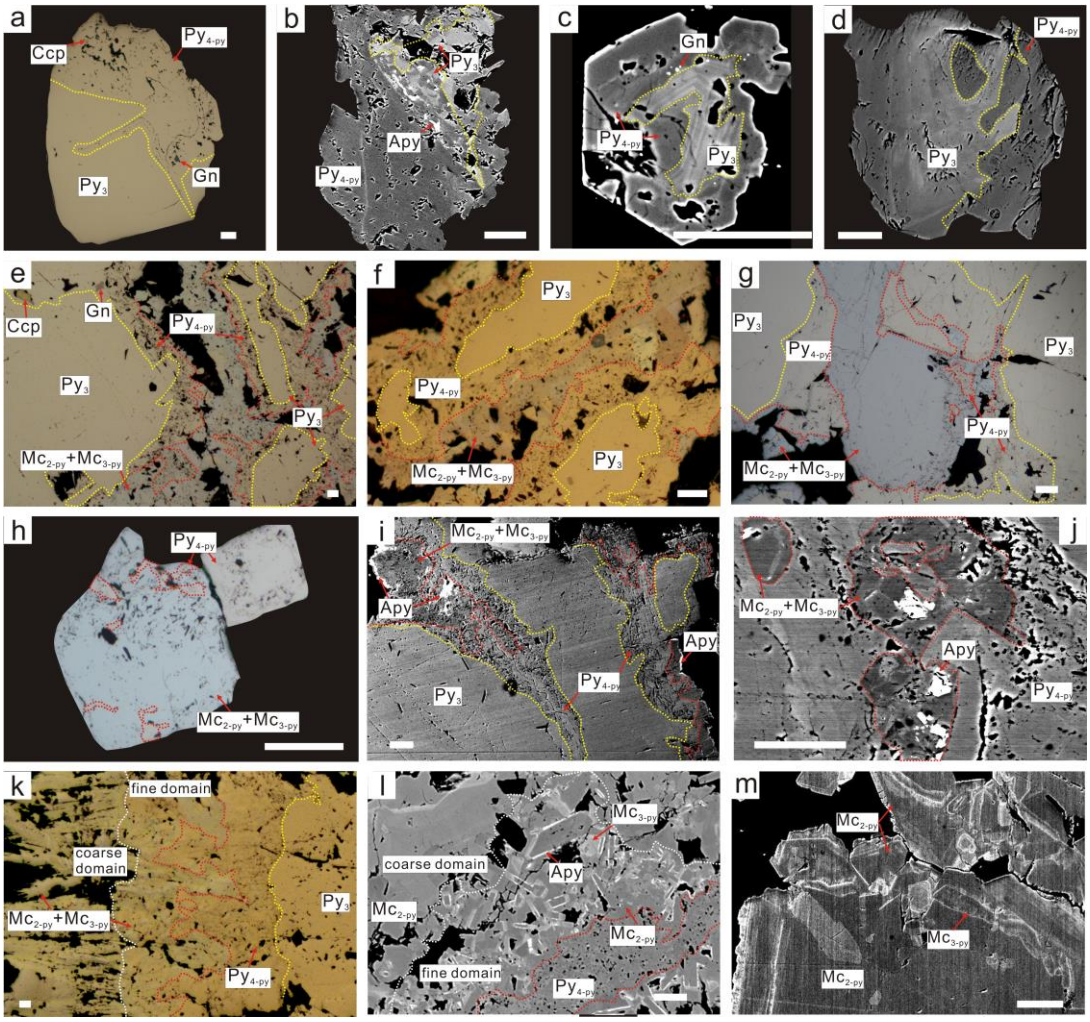
a
Ccp
Py4-py
Py3
Gn
b
Py3
Apy
Py4-py
c
Gn
Py4-py
Py3
d
Py4-py
Py3
e
Ccp
Gn
Py4-py
Py3
Py3
Mc2-py+Mc3-py
f
Py3
Py4-py
Mc2-py+Mc3-py
Py3
g
Py3
Py4-py
Py3
Py4-py
Mc2-py+Mc3-py
h
Py4-py
Mc2-py+Mc3-py
i
Mc2-py+Mc3-py
Apy
Apy
Py3
Py4-py
j
Mc2-py+Mc3-py
Apy
Py4-py
k
fine domain
coarse domain
Py3
Mc2-py+Mc3-py
Py4-py
l
Mc3-py
coarse domain
Apy
Mc2-py
Mc2-py
fine domain
Py4-py
m
Mc2-py
Mc3-py
Mc2-py

**Fig. 4**

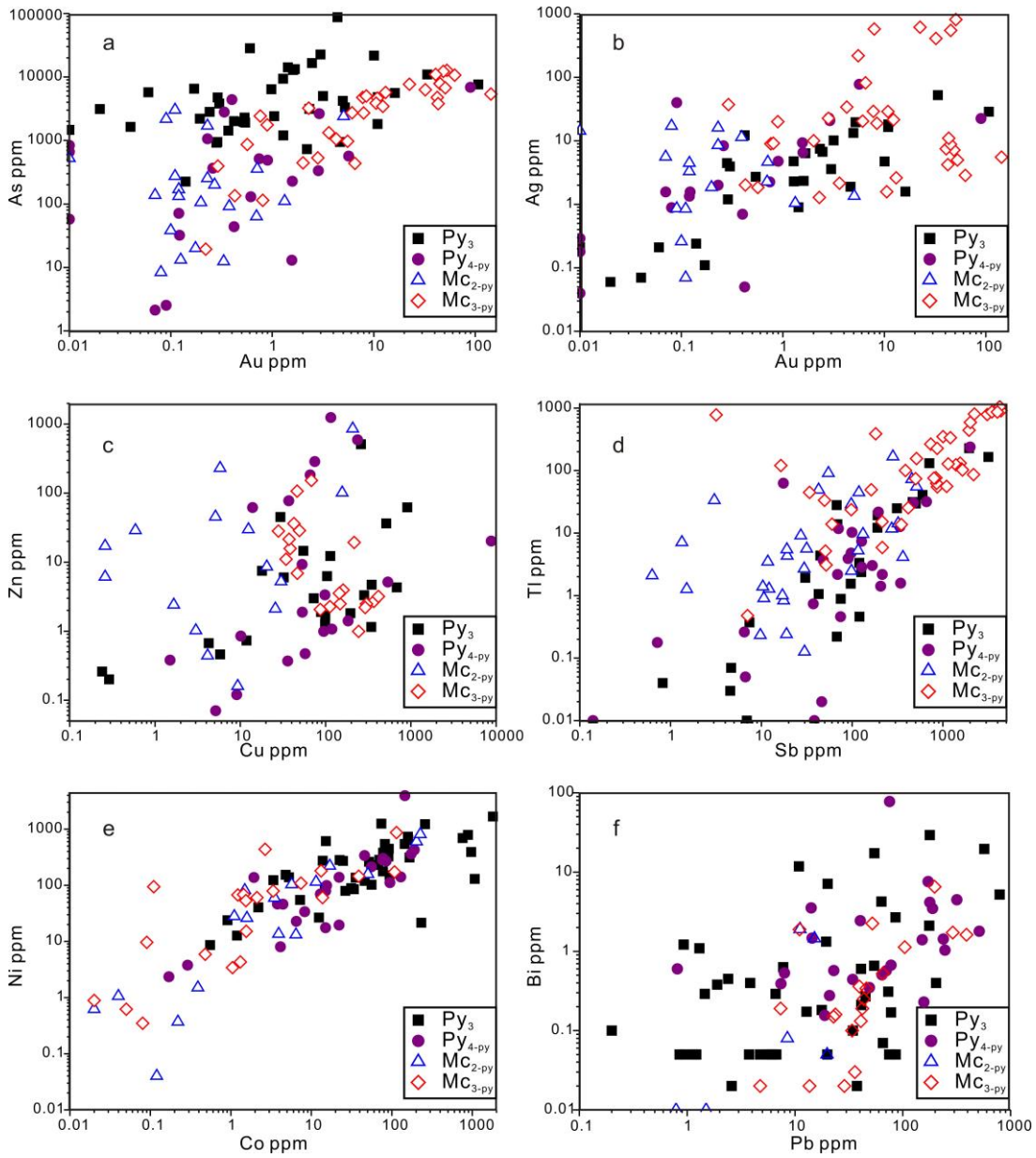
a
As ppm
Au ppm
b
Ag ppm
Au ppm
c
Zn ppm
Cu ppm
d
Tl ppm
Sb ppm
e
Ni ppm
Co ppm
f
Bi ppm
Pb ppm
Py3
Py4-py
Mc2-py
Mc3-py

**Fig. 5**

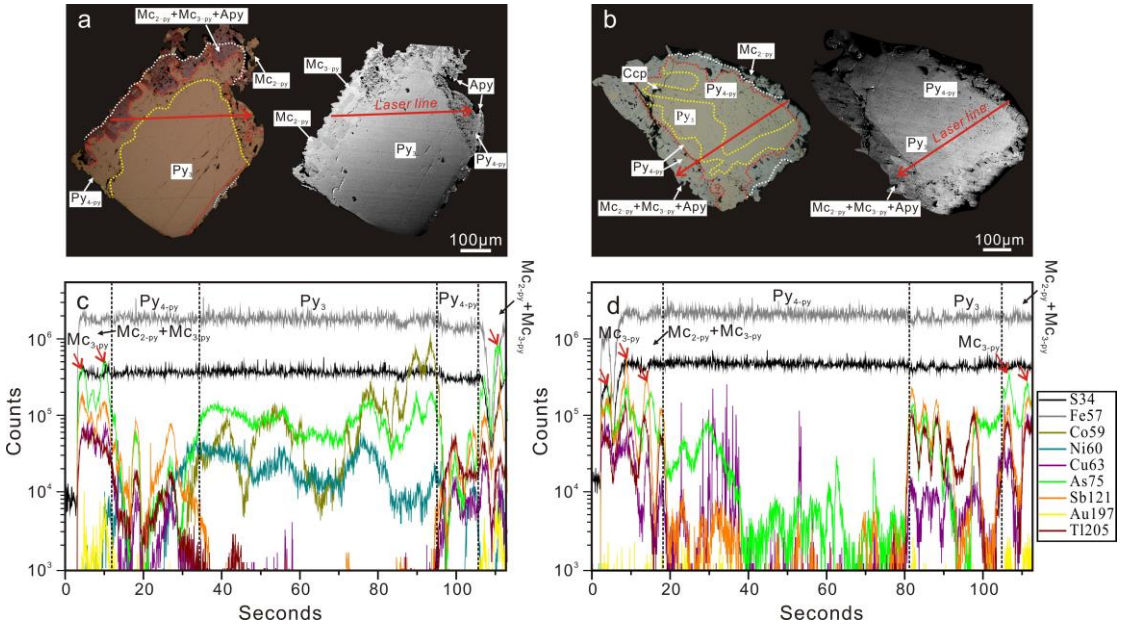
a
b
Laser line
100μm
c
d
Py4-py
Py3
Mc2-py+Mc3-py
Mc3-py
Counts
Seconds
S34
Fe57
Co59
Ni60
Cu63
As75
Sb121
Au197
Tl205

**Fig. 6**

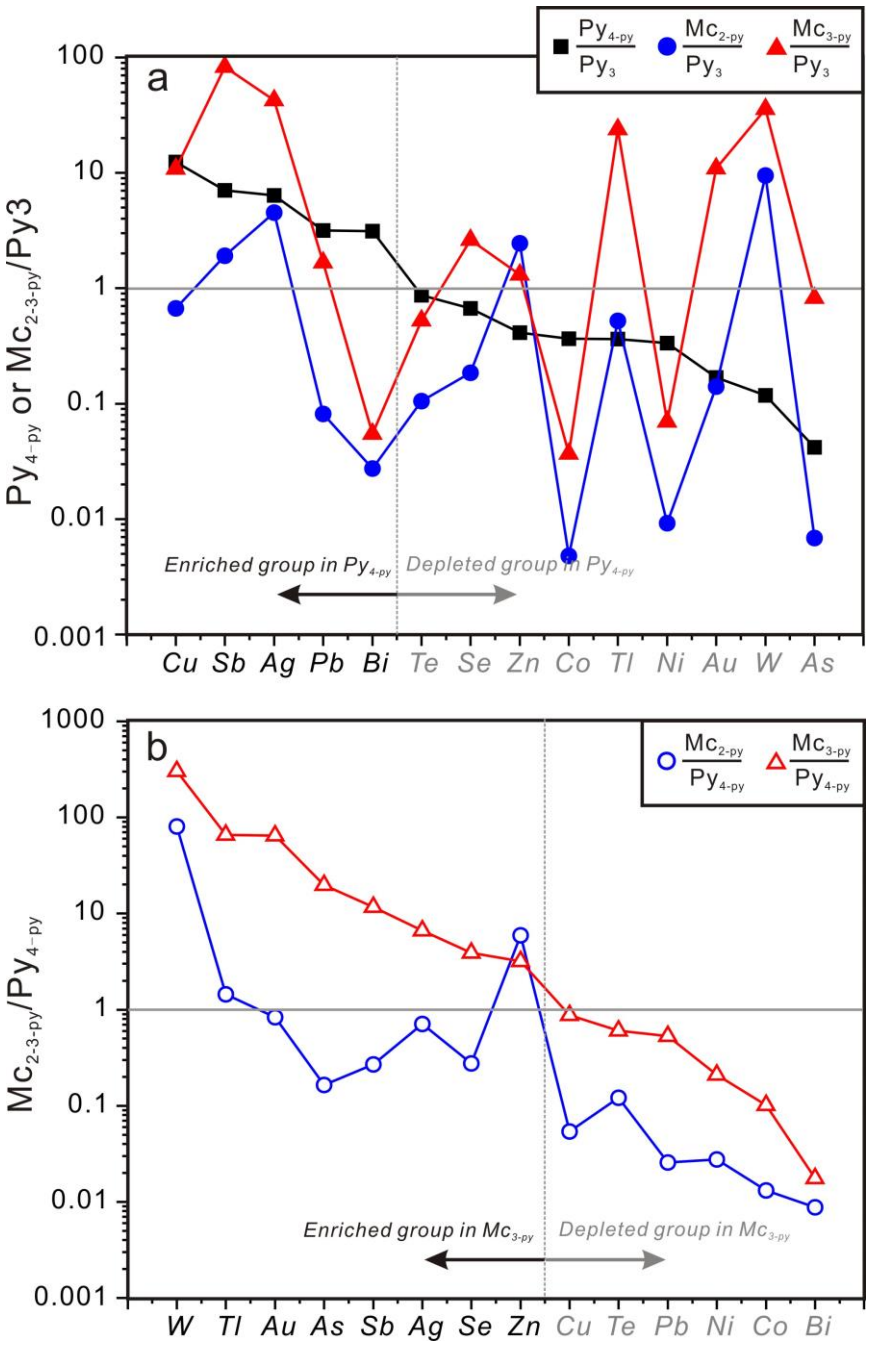
a
$Py_{4\text{-}py}/Py_3$
$Mc_{2\text{-}py}/Py_3$
$Mc_{3\text{-}py}/Py_3$
$Py_{4\text{-}py}$ or $Mc_{2\text{-}3\text{-}py}/Py3$
100
10
1
0.1
0.01
0.001
Enriched group in $Py_{4\text{-}py}$
Depleted group in $Py_{4\text{-}py}$
Cu Sb Ag Pb Bi Te Se Zn Co Tl Ni Au W As
b
$Mc_{2\text{-}py}/Py_{4\text{-}py}$
$Mc_{3\text{-}py}/Py_{4\text{-}py}$
$Mc_{2\text{-}3\text{-}py}/Py_{4\text{-}py}$
1000
100
10
1
0.1
0.01
0.001
Enriched group in $Mc_{3\text{-}py}$
Depleted group in $Mc_{3\text{-}py}$
W Tl Au As Sb Ag Se Zn Cu Te Pb Ni Co Bi

**Fig. 7**

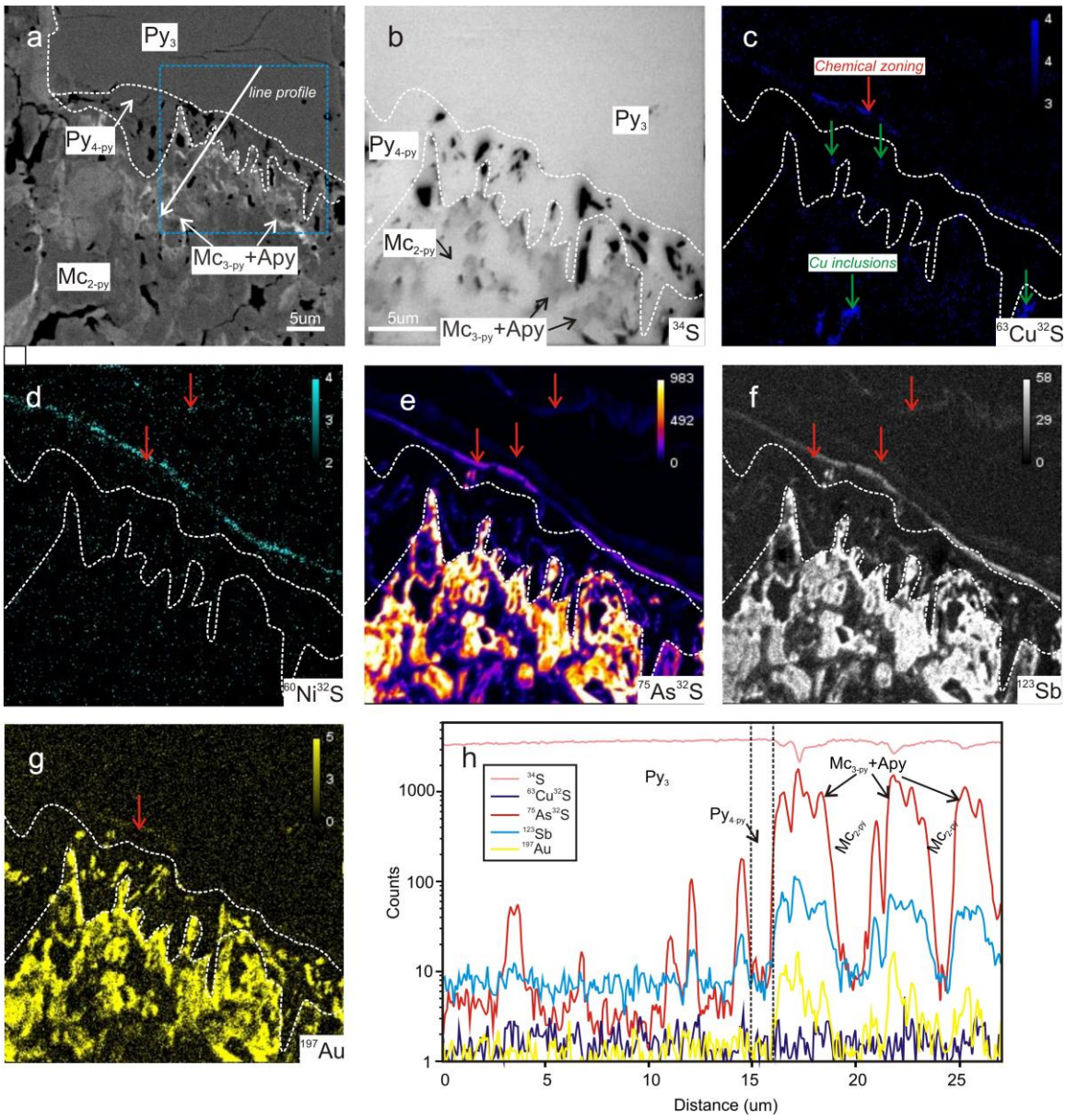
a
Py3
line profile
Py4-py
Mc3-py+Apy
Mc2-py
5um
b
Py3
Py4-py
Mc2-py
5um
Mc3-py+Apy
34S
c
Chemical zoning
Cu inclusions
63Cu32S
d
60Ni32S
e
75As32S
f
123Sb
g
197Au
h
34S
63Cu32S
75As32S
123Sb
197Au
Py3
Py4-py
Mc3-py+Apy
Mc2-py
Mc2-py
Counts
Distance (um)

**Fig. 8**

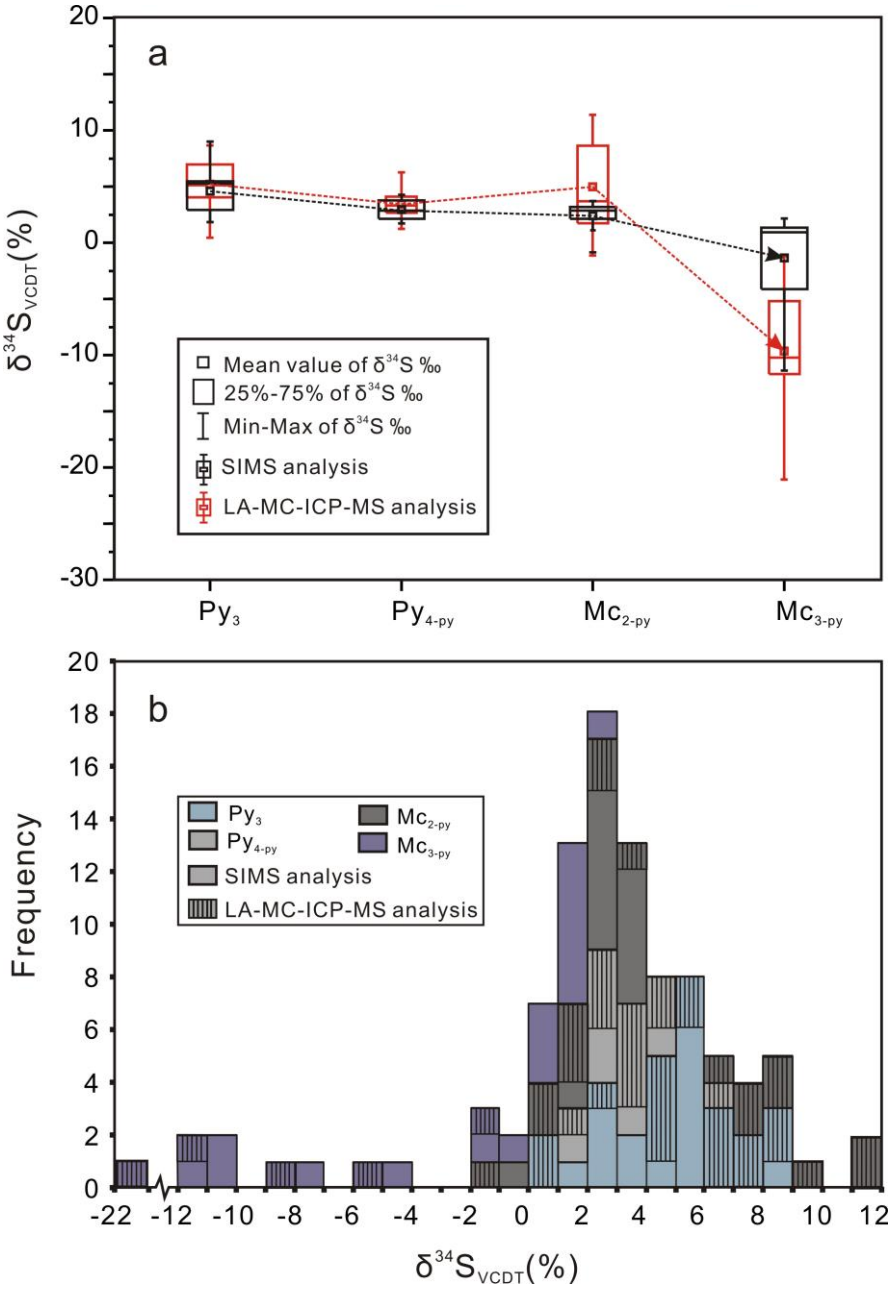
a
20
10
0
-10
-20
-30
$\delta^{34}S_{VCDT}(\%)$
Mean value of $\delta^{34}S$ ‰
25%-75% of $\delta^{34}S$ ‰
Min-Max of $\delta^{34}S$ ‰
SIMS analysis
LA-MC-ICP-MS analysis
$Py_3$
$Py_{4\text{-}py}$
$Mc_{2\text{-}py}$
$Mc_{3\text{-}py}$
b
Frequency
20
18
16
14
12
10
8
6
4
2
0
$Py_3$
$Py_{4\text{-}py}$
$Mc_{2\text{-}py}$
$Mc_{3\text{-}py}$
SIMS analysis
LA-MC-ICP-MS analysis
-22 -12 -10 -8 -6 -4 -2 0 2 4 6 8 10 12
$\delta^{34}S_{VCDT}(\%)$

**Fig. 9**

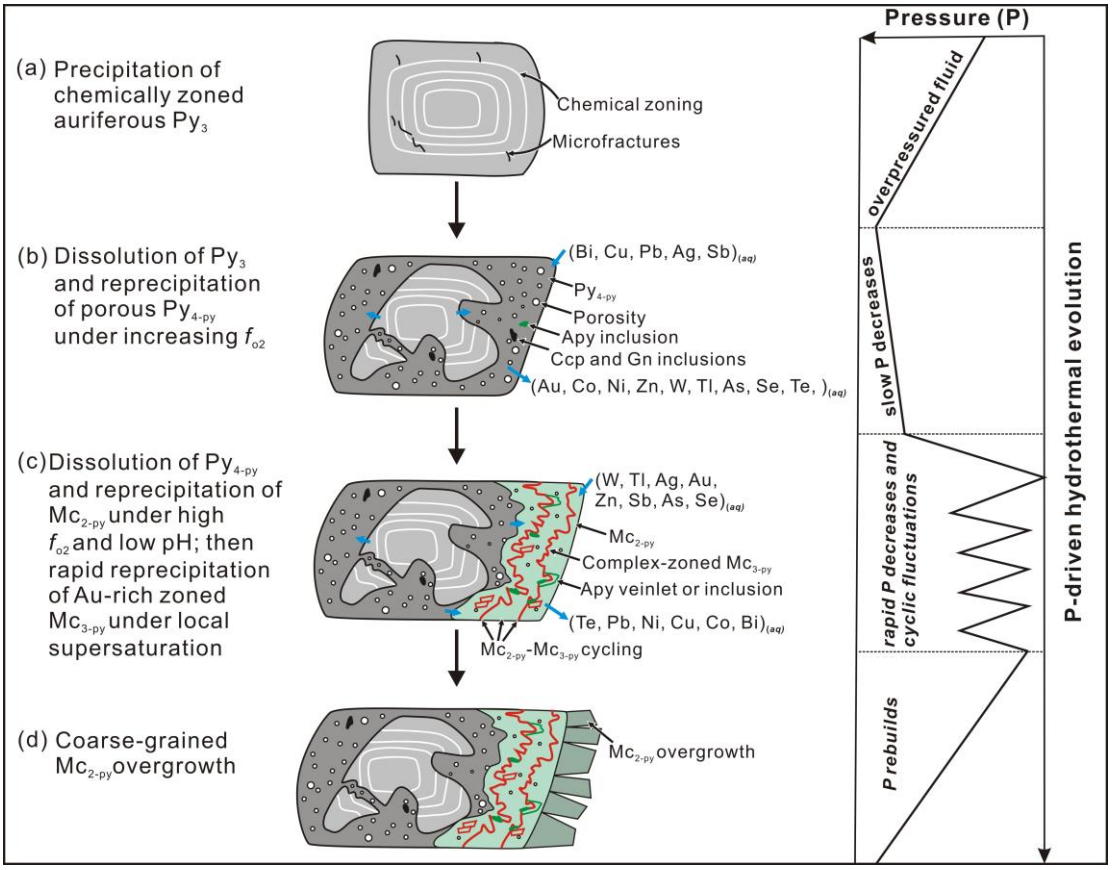
(a) Precipitation of chemically zoned auriferous $Py_3$
Chemical zoning
Microfractures
(b) Dissolution of $Py_3$ and reprecipitation of porous $Py_{4\text{-}py}$ under increasing $f_{o2}$
$(Bi, Cu, Pb, Ag, Sb)_{(aq)}$
$Py_{4\text{-}py}$
Porosity
Apy inclusion
Ccp and Gn inclusions
$(Au, Co, Ni, Zn, W, Tl, As, Se, Te, )_{(aq)}$
(c)Dissolution of $Py_{4\text{-}py}$ and reprecipitation of $Mc_{2\text{-}py}$ under high $f_{o2}$ and low pH; then rapid reprecipitation of Au-rich zoned $Mc_{3\text{-}py}$ under local supersaturation
$(W, Tl, Ag, Au, Zn, Sb, As, Se)_{(aq)}$
$Mc_{2\text{-}py}$
Complex-zoned $Mc_{3\text{-}py}$
Apy veinlet or inclusion
$(Te, Pb, Ni, Cu, Co, Bi)_{(aq)}$
$Mc_{2\text{-}py}$-$Mc_{3\text{-}py}$ cycling
(d) Coarse-grained $Mc_{2\text{-}py}$ overgrowth
$Mc_{2\text{-}py}$ overgrowth
Pressure (P)
Overpressured fluid
slow P decreases
rapid P decreases and cyclic fluctuations
P rebuilds
P-driven hydrothermal evolution

**Table 1. Comparison between diagnostic features of dissolution and reprecipitation, overgrowth, solid-state**

| Main features | Dissolution and reprecipitation | Overgrowth | Solid-state diffusion | Sulfide textures at Daqiao gold deposit |
|---|---|---|---|---|
| Preservation of external morphology | tight (dissolution-limiting) or rough (reprecipitation-limiting) preservation of external morphology of parent phase | overgrowth phase coarsens the external morphology of pre-existing phase | preservation of external morphology of parent phase | some aspects of preservation of external morphology of $Py_3$ and $Py_{4\text{-}py}$ |
| Phase boundary | distinct and sharp interface between parent and product phases | sharp interface between pre-existing and overgrowth phase | compositional diffusion gradients caused by ion exchange in both parent and product phases | distinct and sharp interfaces even at sub-micron scale |
| Porosity | numerous permeable pores and cracks within product phase | few pores in overgrowth phase; pores exist during rapid growth | few pores within product phase | numerous pores within $Py_{4\text{-}py}$, aggregates of $Mc_{2\text{-}py}$ and $Mc_{3\text{-}py}$; few pores in coarse-grained $Mc_{2\text{-}py}$ |
| Mineral inclusion | numerous mineral inclusions in product phase | existence or absence of inclusions | absence of inclusions | chalcopyrite, galena, and arsenopyrite inclusions within $Py_{4\text{-}py}$; arsenopyrite inclusion within aggregates of $Mc_{2\text{-}py}$ and $Mc_{3\text{-}py}$ |
| Existence of fluid | fluid-involved open system | fluid-involved open system | dry and closed system | episodic infiltration of deep-seated hydrothermal fluids |
| Temperature | low to high temperature | low to high temperature | high temperature (e.g., 425–500 ℃) | low temperature (< 240 ℃) |
| Reaction rate | rapid (e.g., several hours) | rapid (e.g., several hours) | extremely slow (e.g., millions of years) | relative rapid related to hydraulic fracturing |

**Table 2. Summarized LA-ICP-MS analyses of different generations of pyrite and marcasite involved in the pyrite replacement from the Daqiao gold deposit.**

| Iron sulfides | Co | Ni | Cu | Zn | As | Se | Ag | Sb | Te | W | Au | Tl | Pb | Bi |
|---|---|---|---|---|---|---|---|---|---|---|---|---|---|---|
| **$Py_3$** (*n* = 49) | | | | | | | | | | | | | | |
| Median | 35.6 | 138.8 | 4.3 | 3.0 | 3115.1 | 54.4 | 0.2 | 10.0 | 0.2 | 0.9 | 0.53 | 4.4 | 12.8 | 0.2 |
| Min | b.d.l. | b.d.l. | b.d.l. | b.d.l. | b.d.l. | b.d.l. | b.d.l. | b.d.l. | b.d.l. | b.d.l. | b.d.l. | b.d.l. | 2.9 | b.d.l. |
| Max | 1805.7 | 1679.2 | 905.3 | 511.6 | 87443.9 | 464.5 | 52.3 | 3172.9 | 18.5 | 15.4 | 107.01 | 227.2 | 791.1 | 29.3 |
| **$Py_{4\text{-}py}$** (*n* = 33) | | | | | | | | | | | | | | |
| Median | 13.0 | 46.5 | 53.0 | 1.2 | 130.2 | 36.5 | 1.3 | 70.6 | 0.2 | 0.1 | 0.09 | 1.6 | 40.4 | 0.6 |
| Min | b.d.l. | b.d.l. | b.d.l. | b.d.l. | b.d.l. | b.d.l. | b.d.l. | b.d.l. | b.d.l. | b.d.l. | b.d.l. | b.d.l. | 2.9 | b.d.l. |
| Max | 190.2 | 3949.7 | 8730.3 | 1246.8 | 8031.4 | 124.4 | 78.0 | 1999.8 | 20.1 | 7.4 | 89.85 | 238.0 | 2163.7 | 166.3 |
| **$Mc_{2\text{-}py}$** (*n* = 44) | | | | | | | | | | | | | | |
| Median | 0.2 | 1.3 | 2.9 | 7.4 | 21.4 | 10.1 | 1.0 | 19.1 | 0.0 | 8.8 | 0.08 | 2.3 | 1.0 | 0.0 |
| Min | b.d.l. | b.d.l. | b.d.l. | b.d.l. | b.d.l. | b.d.l. | b.d.l. | b.d.l. | b.d.l. | b.d.l. | b.d.l. | b.d.l. | 2.9 | b.d.l. |
| Max | 226.3 | 809.7 | 250.9 | 856.7 | 3028.4 | 131.3 | 17.1 | 514.1 | 6.6 | 462.7 | 5.06 | 167.3 | 151.4 | 1.9 |
| **$Mc_{3\text{-}py}$** (*n* = 40) | | | | | | | | | | | | | | |
| Median | 1.3 | 9.7 | 46.5 | 3.9 | 2578.2 | 142.4 | 8.9 | 824.2 | 0.1 | 33.2 | 5.82 | 104.1 | 21.4 | 0.0 |
| Min | b.d.l. | b.d.l. | b.d.l. | b.d.l. | 19.4 | 3.6 | b.d.l. | 3.2 | b.d.l. | b.d.l. | b.d.l. | 0.5 | 2.9 | b.d.l. |
| Max | 114.5 | 872.0 | 415.2 | 519.4 | 12726.5 | 427.6 | 815.6 | 4369.8 | 9.2 | 92.7 | 62.86 | 1049.6 | 720.7 | 6.5 |

**Table B.1. LA-ICP-MS analyses of different generations of pyrite and marcasite involved in the pyrite replacement from the Daqiao gold deposit**

| Sample no. | Analysis no. | Iron Sulfides | Co | Ni | Cu | Zn | As | Se | Ag | Sb | Te | W | Au | Tl | Pb | Bi |
|---|---|---|---|---|---|---|---|---|---|---|---|---|---|---|---|---|
| DQ391-1 | DQ391-1 | | 13.82 | 273.92 | 4.27 | 0.67 | 3133.08 | 78.99 | 0.06 | 4.65 | 0.19 | 0.01 | 0.02 | 0.07 | 7.79 | 0.63 |
| DQ391-2 | DQ391-2 | | 93.64 | 150.49 | 32.39 | 6.03 | 5729.82 | 70.28 | 0.21 | 42.80 | 0.04 | 0.04 | 0.06 | 1.06 | 54.32 | 0.66 |
| DQ447-1 | DQ447-1 | | 1.19 | 12.74 | 103.83 | 6.26 | 21746.89 | 283.64 | 4.74 | 126.27 | 0.00 | 0.93 | 10.05 | 2.38 | 18.67 | 0.00 |
| DQ447-2 | DQ447-2 | | 5.28 | 138.83 | 72.46 | 3.00 | 5026.65 | 50.27 | 10.15 | 463.18 | 0.28 | 5.22 | 3.16 | 31.28 | 74.69 | 0.05 |
| DQ462-1 | DQ462-1 | | 15.17 | 610.84 | 5.79 | 0.46 | 6516.35 | 1.66 | 0.11 | 6.93 | 0.15 | 2.52 | 0.17 | 0.01 | 6.60 | 0.29 |
| DQ462-2 | DQ462-2 | | 258.02 | 1225.82 | 99.13 | 1.66 | 9392.46 | 2.58 | 4.78 | 67.72 | 0.90 | 0.17 | 1.28 | 0.22 | 45.02 | 0.27 |
| DQ445-1 | DQ445-1 | | 52.26 | 261.61 | 54.85 | 14.62 | 1816.96 | 52.50 | 16.51 | 709.33 | 0.00 | 1.75 | 10.90 | 130.88 | 34.44 | 0.10 |
| DQ-107-3 | DQ-107-3 | | 0.55 | 8.64 | 29.54 | 45.23 | 2010.46 | 1.53 | 12.26 | 67.59 | 0.00 | 2.84 | 0.42 | 28.06 | 2.59 | 0.02 |
| DQ-282-1 | DQ-282-1 | $Py_3$ | 55.91 | 102.28 | 11.80 | 0.73 | 225.38 | 42.10 | 0.24 | 4.54 | 0.23 | 0.00 | 0.14 | 0.03 | 20.08 | 7.12 |
| DQ-291-2 | DQ-291-2 | | 7.23 | 54.87 | 342.49 | 1.15 | 4812.63 | 54.37 | 18.17 | 190.31 | 0.11 | 0.80 | 10.93 | 12.22 | 41.00 | 0.60 |
| DQ-291-5 | DQ-291-5 | | 12.43 | 26.63 | 195.29 | 1.82 | 3317.96 | 33.93 | 19.67 | 311.23 | 0.10 | 0.40 | 5.21 | 24.85 | 73.26 | 0.31 |
| DQ-383-1 | DQ-383-1 | | 970.49 | 392.25 | 0.24 | 0.26 | 1637.62 | 77.07 | 0.07 | 0.82 | 0.00 | 0.03 | 0.04 | 0.04 | 1.46 | 0.29 |
| DQ-288-1 | DQ-288-1 | | 82.12 | 542.62 | 113.66 | 12.26 | 4215.92 | 71.85 | 13.33 | 596.29 | 1.87 | 1.20 | 4.95 | 40.76 | 63.44 | 4.24 |
| DQ-288-2 | DQ-288-2 | | 91.71 | 448.34 | 513.18 | 36.41 | 10967.87 | 126.98 | 52.30 | 3172.87 | 4.04 | 2.67 | 33.66 | 164.63 | 569.17 | 19.53 |
| DQ-379-3 | DQ-379-3 | | 144.84 | 543.93 | 0.29 | 0.20 | 2565.18 | 31.31 | 0.03 | 0.73 | 0.18 | 0.03 | 0.00 | 0.00 | 1.30 | 1.09 |
| DQ-379-6 | DQ-379-6 | | 78.10 | 379.20 | 282.76 | 3.32 | 3143.03 | 13.94 | 7.51 | 190.74 | 7.05 | 0.15 | 2.32 | 19.31 | 178.00 | 29.27 |

| | | | | | | | | | | | | | | | |
|---|---|---|---|---|---|---|---|---|---|---|---|---|---|---|---|
| DQ-379-7 | DQ-379-7 | | 74.25 | 1248.61 | 905.31 | 62.21 | 3827.86 | 20.95 | 3.96 | 68.64 | 3.08 | 0.37 | 0.30 | 13.86 | 10.87 | 11.83 |
| DQ-395-1 | DQ-395-1 | | 90.72 | 326.78 | 18.01 | 7.48 | 1472.57 | 6.48 | 0.21 | 44.53 | 0.19 | 8.73 | 0.01 | 4.36 | 791.14 | 5.22 |
| DQ-477-1 | DQ-477-1 | | 0.91 | 23.86 | 98.45 | 1.27 | 22624.49 | 458.31 | 3.59 | 30.53 | 6.03 | 0.01 | 2.99 | 1.93 | 37.65 | 0.02 |
| DQ-477-2 | DQ-477-2 | | 160.49 | 649.19 | 98.77 | 1.23 | 13345.52 | 464.46 | 6.38 | 120.69 | 8.34 | 1.35 | 1.67 | 0.46 | 203.38 | 0.40 |
| DQ-477-3 | DQ-477-3 | | 3.37 | 123.42 | 88.52 | 1.90 | 16560.87 | 437.39 | 6.73 | 96.55 | 5.31 | 12.70 | 2.46 | 1.55 | 65.31 | 0.07 |
| DQ-198-1 | DQ-198-1 | | 4.79 | 153.74 | 346.96 | 4.71 | 5584.95 | 139.46 | 1.59 | 503.80 | 0.06 | 9.79 | 16.13 | 29.73 | 41.15 | 0.21 |
| DQ-198-7 | DQ-198-7 | | 35.55 | 137.14 | 682.38 | 4.31 | 7613.33 | 122.05 | 28.73 | 1944.06 | 0.06 | 1.07 | 107.01 | 227.24 | 77.82 | 0.17 |
| DQ403-1 | DQ403-1 | | 3.79 | 46.45 | 13.95 | 62.12 | 43.79 | 3.66 | 0.05 | 342.66 | 0 | 0 | 0.42 | 1.58 | 6.41 | 0 |
| DQ429-2 | DQ429-2 | | 22.16 | 138.49 | 57.5 | 0.47 | 2.13 | 27.34 | 1.57 | 206.54 | 0.3 | 0.02 | 0.07 | 1.41 | 511.58 | 1.79 |
| DQ445-2 | DQ445-2 | | 55.76 | 213.94 | 53.06 | 9.31 | 489.15 | 11.63 | 4.77 | 99.46 | 0.04 | 4.91 | 0.9 | 10.3 | 237.58 | 1.43 |
| DQ445-3 | DQ445-3 | | 45.81 | 337.63 | 98.21 | 3.36 | 365.51 | 3.19 | 8.34 | 126.99 | 0.34 | 0.14 | 0.26 | 7.39 | 317.18 | 4.47 |
| DQ-282-2 | DQ-282-2 | | 13.71 | 62.87 | 1.5 | 0.38 | 57.7 | 61.9 | 0.04 | 0.14 | 0.37 | 0 | 0.01 | 0.01 | 0.81 | 0.6 |
| DQ-291-4 | DQ-291-4 | | 8.29 | 33.95 | 183.61 | 1.41 | 2642.29 | 52.93 | 20.86 | 473.36 | 0 | 6.2 | 2.91 | 30.33 | 77.74 | 0.67 |
| DQ-383-2 | DQ-383-2 | | 1.93 | 137.9 | 53.27 | 1.88 | 71.36 | 3.99 | 1.34 | 70.56 | 0 | 0.51 | 0.12 | 11.82 | 70.18 | 0.57 |
| DQ-263-1-1 | DQ-263-1-1 | $Py_{4\text{-}py}$ | 173.92 | 362.17 | 9.08 | 0.12 | 0.32 | 34.04 | 0.89 | 46.19 | 1.15 | 0 | 0.08 | 0.02 | 177.76 | 4.15 |
| DQ-263-1-2 | DQ-263-1-2 | | 77.51 | 300.39 | 118.67 | 1.07 | 13.04 | 37.08 | 9.32 | 1126.52 | 2.24 | 0 | 1.56 | 0.12 | 2163.71 | 166.32 |
| DQ-263-2-3 | DQ-263-2-3 | | 145.27 | 3949.73 | 8730.3 | 20.25 | 2.53 | 37.24 | 40.03 | 6.66 | 0 | 0.01 | 0.09 | 0.05 | 189.01 | 3.48 |
| DQ-263-2-4 | DQ-263-2-4 | | 0.17 | 2.35 | 5.14 | 0.07 | 0 | 35.88 | 0.36 | 0.05 | 0.12 | 0 | 0 | 0 | 7.42 | 0.39 |
| DQ-355-1 | DQ-355-1 | | 4.13 | 8.01 | 10.14 | 0.85 | 662.86 | 50.3 | 0.18 | 9.77 | 0 | 0.19 | 0.01 | 0 | 49.03 | 0.35 |
| DQ-355-2 | DQ-355-2 | | 0.29 | 3.79 | 36.98 | 77.64 | 838.79 | 25.88 | 0.29 | 38.33 | 0.21 | 0.25 | 0.01 | 0.01 | 151.2 | 1.4 |
| DQ-198-6 | DQ-198-6 | | 85.03 | 269.03 | 536.5 | 5.15 | 6901.95 | 102.1 | 22.49 | 1999.7 | 0.01 | 3.59 | 89.85 | 237.96 | 156.82 | 0.23 |

| | | | | | | | | | 3 | | 7 | | | | | |
|---|---|---|---|---|---|---|---|---|---|---|---|---|---|---|---|---|
| DQ382-1 | DQ382-1 | | 94.81 | 111.14 | 35.84 | 0.37 | 4416.88 | 59.77 | 0.7 | 97.31 | 20.08 | 0.08 | 0.4 | 4.79 | 75.57 | 77.78 |
| DQ382-2 | DQ382-2 | | 76.88 | 281.83 | 94.8 | 0.99 | 1063.69 | 47.1 | 2 | 90.21 | 0.96 | 1.02 | 0.23 | 3.9 | 14.13 | 3.53 |
| DQ403-2 | DQ403-2 | | 1.58 | 25.95 | 5.8 | 230.94 | 0.16 | 3.48 | 0.04 | 18.98 | 0 | 0 | 0 | 0.24 | 0.86 | 0 |
| DQ429-1 | DQ429-1 | | 1.1 | 28 | 25.72 | 2.11 | 38.37 | 8.03 | 0.26 | 3.04 | 0.04 | 3.7 | 0.1 | 33.47 | 0.6 | 0 |
| DQ462-3 | DQ462-3 | | 50.56 | 157.41 | 156.29 | 101.79 | 524.79 | 2.13 | 14.3 | 272.52 | 0.05 | 462.72 | 0.01 | 11.69 | 151.43 | 0.02 |
| DQ-107-2 | DQ-107-2 | | 0.04 | 1.06 | 12.45 | 29.84 | 1701.41 | 2.96 | 8.53 | 42.76 | 0 | 0.31 | 0.23 | 49.36 | 1.5 | 0.01 |
| DQ-395-2 | DQ-395-2 | | 0.22 | 0.37 | 30.07 | 5.25 | 273.27 | 2.67 | 0.07 | 97.74 | -0.05 | 25.78 | 0.11 | 28.84 | 19.9 | 0.05 |
| DQ-198-9 | DQ-198-9 | | 0.39 | 1.5 | 20.42 | 8.59 | 2393.31 | 131.29 | 1.35 | 131.92 | 0.16 | 83.28 | 5.06 | 9.62 | 8.52 | 0.08 |
| DQ-208-1 | DQ-208-1 | $Mc_{2\text{-}py}$ | 0 | 1.06 | 5.11 | 45.49 | 253 | 5.93 | 16.05 | 362.55 | 0 | 12.81 | 0.23 | 4.13 | 1.03 | 0 |
| DQ-208-5 | DQ-208-5 | | 0 | 0.03 | 0.59 | 28.98 | 169.59 | 55.48 | 3.3 | 455.01 | 0 | 36.69 | 0.12 | 72.8 | 0.54 | 0 |
| DQ-208-7 | DQ-208-7 | | 0.02 | 0.62 | 3.02 | 1.02 | 8.38 | 1.54 | 17.14 | 11.77 | 0 | 0.25 | 0.08 | 3.47 | 0.26 | 0 |
| DQ-209-2 | DQ-209-2 | | 0.12 | 0.04 | 0.26 | 17.16 | 132.45 | 83.68 | 4.47 | 514.05 | 0.08 | 10.75 | 0.12 | 55.22 | 1.86 | 0 |
| DQ-209-3 | DQ-209-3 | | 0 | 0 | 0.26 | 6.12 | 137.68 | 20.19 | 5.59 | 31.53 | 0 | 7.15 | 0.07 | 5.62 | 0.79 | 0.01 |
| DQ-209-4 | DQ-209-4 | | 0.01 | 0 | 1.66 | 2.41 | 357.02 | 12.09 | 4.65 | 118.87 | 0 | 10.52 | 0.71 | 44.57 | 3.96 | 0 |
| DQ-379-1 | DQ-379-1 | | 203.25 | 596.71 | 9.36 | 0.16 | 2176.12 | 20.69 | 0.86 | 19.34 | 0.23 | 0 | 0.09 | 4.32 | 11.13 | 1.9 |
| DQ-379-2 | DQ-379-2 | | 226.32 | 809.66 | 4.15 | 0.44 | 3028.36 | 28.75 | 0.85 | 12.15 | 0.19 | 0.03 | 0.11 | 1.28 | 15.17 | 1.45 |
| DQ-107-1 | DQ-107-1 | | 1.55 | 15.18 | 42.48 | 36.28 | 1758.77 | 3.58 | 19.97 | 49.73 | 0.1 | 10.38 | 0.89 | 33.53 | 7.36 | 0.19 |
| DQ-282-3 | DQ-282-3 | | 0 | 7.07 | 367.64 | 2.69 | 2437.23 | 149.9 | 9 | 1550.65 | 0.55 | 45.55 | 0.76 | 131.23 | 28.7 | 0.02 |
| DQ-291-3 | DQ-291-3 | $Mc_{3\text{-}py}$ | 13.2 | 180.75 | 86.65 | 2.06 | 4625.02 | 37.09 | 29 | 868.37 | 0.49 | 33.19 | 10.87 | 54.66 | 197.2 | 6.51 |
| DQ-291-1 | DQ-291-1 | | 1.22 | 67.46 | 112.43 | 2.26 | 4749.37 | 96.33 | 29.12 | 1097.33 | 0.17 | 44.49 | 7.79 | 55.91 | 104.53 | 1.13 |
| DQ-383-3 | DQ-383-3 | | 0.11 | 94.26 | 244.08 | 0.99 | 3240.15 | 60.72 | 1.28 | 500.18 | 0.28 | 18.69 | 2.29 | 74.14 | 33.91 | 0.1 |

| | | | | | | | | | | | | | | | |
|---|---|---|---|---|---|---|---|---|---|---|---|---|---|---|---|
| DQ-379-4 | DQ-379-4 | | 108.27 | 172.8 | 415.16 | 3.18 | 5009.62 | 36.02 | 18.95 | 511.5 | 1.19 | 3.52 | 8.46 | 155.61 | 11.03 | 1.89 |
| DQ-379-5 | DQ-379-5 | | 2.67 | 436.92 | 148.13 | 2.49 | 2728.77 | 18.53 | 20.48 | 387.49 | 0.49 | 3.29 | 6.11 | 100.41 | 52.27 | 2.25 |
| DQ-198-2 | DQ-198-2 | | 2.11 | 60.22 | 300.88 | 2.48 | 12726.47 | 301.58 | 4.98 | 1389.27 | 0.01 | 5.6 | 52.61 | 123.55 | 43.51 | 0.25 |
| DQ-198-3 | DQ-198-3 | | 1.44 | 68.41 | 290.61 | 2.2 | 10708.14 | 241.6 | 2.87 | 852.11 | 0 | 17.25 | 62.86 | 62.47 | 23.74 | 0.16 |
| DQ-198-4 | DQ-198-4 | | 1.54 | 53.2 | 160.02 | 3.94 | 12217.57 | 305.05 | 7.16 | 1610.6 | 0.06 | 35.97 | 48.47 | 106.05 | 39.51 | 0.36 |
| DQ-198-5 | DQ-198-5 | | 3.35 | 78.79 | 144.74 | 3.55 | 10934.02 | 275.2 | 7.51 | 1640.6 | 0.01 | 70.96 | 40.81 | 102.19 | 45.99 | 0.34 |
| DQ-198-8 | DQ-198-8 | | 114.49 | 871.95 | 216.53 | 19.32 | 7870.94 | 109.09 | 8.82 | 2174.47 | 0.33 | 32.76 | 44.89 | 86.41 | 389.78 | 1.62 |
| DQ-198-10 | DQ-198-10 | | 1.31 | 4.31 | 34.43 | 11.02 | 3866.47 | 118.71 | 1.58 | 213.79 | 0 | 92.68 | 10.55 | 15.19 | 22.78 | 0.15 |
| DQ-198-11 | DQ-198-11 | | 1.05 | 3.4 | 46.69 | 6.88 | 5711.13 | 310.1 | 2.61 | 415.07 | 0 | 38.61 | 13.06 | 25.44 | 42.17 | 0.19 |
| DQ-208-2 | DQ-208-2 | | 0.08 | 0.35 | 27.95 | 28.16 | 2719.1 | 108.5 | 577.13 | 4369.77 | 0.18 | 51.7 | 7.96 | 902.78 | 4.76 | 0.02 |
| DQ-208-3 | DQ-208-3 | | 0.02 | 0.89 | 38.49 | 15.73 | 7836.08 | 216.18 | 549.59 | 3085.07 | 0 | 28.72 | 45.05 | 786.7 | 2.47 | 0 |
| DQ-208-4 | DQ-208-4 | | 0.05 | 0.62 | 46.25 | 107.25 | 6736.69 | 142.36 | 815.62 | 4225.72 | 0.04 | 46.52 | 50.68 | 1049.59 | 4.51 | 0 |
| DQ-208-6 | DQ-208-6 | | 0.09 | 9.6 | 49.3 | 28.79 | 7690.66 | 427.63 | 617.36 | 3461.39 | 0.1 | 63.73 | 22.48 | 868.16 | 13.65 | 0.02 |
| DQ-209-1 | DQ-209-1 | | 0.48 | 5.89 | 37.35 | 21.49 | 6279.67 | 189.09 | 409.88 | 1945.33 | 0 | 3.89 | 32.23 | 442.71 | 35.95 | 0.03 |

1162

**Table B.2. SIMS in situ sulfur isotope compositions of different generations of pyrite and marcasite involved in the pyrite replacement from the Daqiao gold deposit**

| Analysis no. | Iron Sulfides | $\delta^{34}S‰_{VCDT}$ | 2s |
|---|---|---|---|
| DQ198-1 | | 2.9 | 0.02 |
| DQ198-7 | | 2.5 | 0.02 |
| DQ291-1 | | 4.1 | 0.02 |
| DQ291-3 | | 4.0 | 0.03 |
| DQ383-1 | | 1.9 | 0.02 |
| DQ379-5 | | 2.3 | 0.02 |
| DQ395-2 | $Py_3$ | 9.0 | 0.03 |
| DQ477-1 | | 5.3 | 0.02 |
| DQ477-2 | | 5.5 | 0.02 |
| DQ477-3 | | 5.3 | 0.02 |
| DQ477-4 | | 5.3 | 0.03 |
| DQ477-5 | | 6.0 | 0.03 |
| DQ477-6 | | 5.5 | 0.03 |
| DQ198-6 | | 4.3 | 0.02 |
| DQ291-4 | | 1.7 | 0.02 |
| DQ383-2 | $Py_{4\text{-}py}$ | 2.1 | 0.02 |
| DQ383-3 | | 2.9 | 0.02 |
| DQ379-2 | | 3.8 | 0.02 |
| DQ198-8 | | 1.1 | 0.02 |
| DQ198-10 | | 3.2 | 0.02 |
| DQ208-1 | | 3.0 | 0.03 |
| DQ208-2 | | 3.7 | 0.03 |
| DQ208-3 | | 2.3 | 0.01 |
| DQ208-6 | | 2.9 | 0.03 |
| DQ291-5 | $Mc_{2\text{-}py}$ | 2.1 | 0.03 |
| DQ291-6 | | 3.3 | 0.02 |
| DQ383-4 | | 2.9 | 0.02 |
| DQ379-1 | | 2.3 | 0.02 |
| DQ379-3 | | 3.2 | 0.03 |
| DQ379-6 | | 2.1 | 0.02 |
| DQ395-1 | | -0.9 | 0.05 |
| DQ198-2 | | 1.3 | 0.03 |
| DQ198-3 | | -1.6 | 0.04 |
| DQ198-4 | | 0.9 | 0.03 |
| DQ198-5 | $Mc_{3\text{-}py}$ | 1.2 | 0.02 |
| DQ198-9 | | 2.2 | 0.02 |
| DQ198-11 | | 1.4 | 0.02 |
| DQ198-12 | | 1.4 | 0.02 |
| DQ198-13 | | 1.5 | 0.02 |

| | | |
|---|---|---|
| DQ198-14 | 1.0 | 0.03 |
| DQ208-4 | 2.0 | 0.02 |
| DQ208-5 | -4.1 | 0.05 |
| DQ208-8 | -8.0 | 0.09 |
| DQ208-7 | -11.4 | 0.14 |
| DQ291-2 | 0.9 | 0.02 |
| DQ379-4 | -10.0 | 0.02 |
| DQ379-7 | -0.1 | 0.08 |

1166